Supplementary Information

Precursor-driven Jahn–Teller distortion as a hidden origin of surface instability in Mn-stabilized Ni-rich cathodes

JinHa Shim,[†] Young Geol Yu,[†] Yu Bin Choi,[†] and Jin Ho Bang*[,†,‡]

[†] Department of Applied Chemistry, Center for Bionano Intelligence Education and Research, Hanyang University ERICA, 55 Hanyangdaehak-ro, Sangnok-gu, Ansan, Gyeonggi-do 15588, Republic of Korea

[‡] Department of Energy and Bio Sciences, Hanyang University ERICA, 55 Hanyangdaehak-ro, Sangnok-gu, Ansan, Gyeonggi-do 15588, Republic of Korea

AUTHOR INFORMATION

Corresponding Author:

*jbang@hanyang.ac.kr

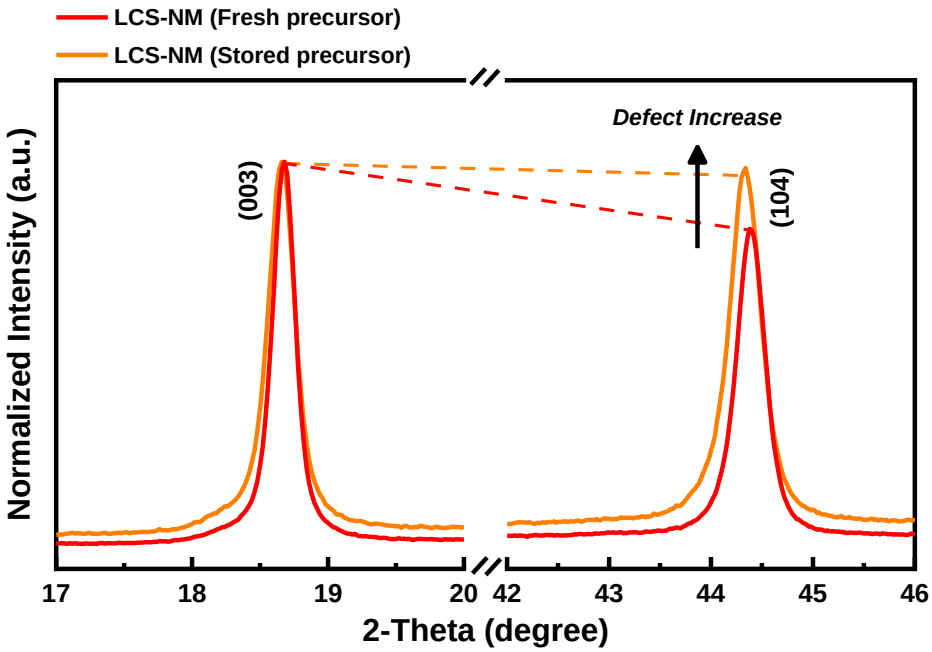

Fig. S1 XRD patterns of LCS-NM synthesized using fresh and stored precursors. The LCS-NM synthesized from the stored precursor exhibits a lower intensity ratio between the (003) and (104) planes, indicating an increase in lattice defects.

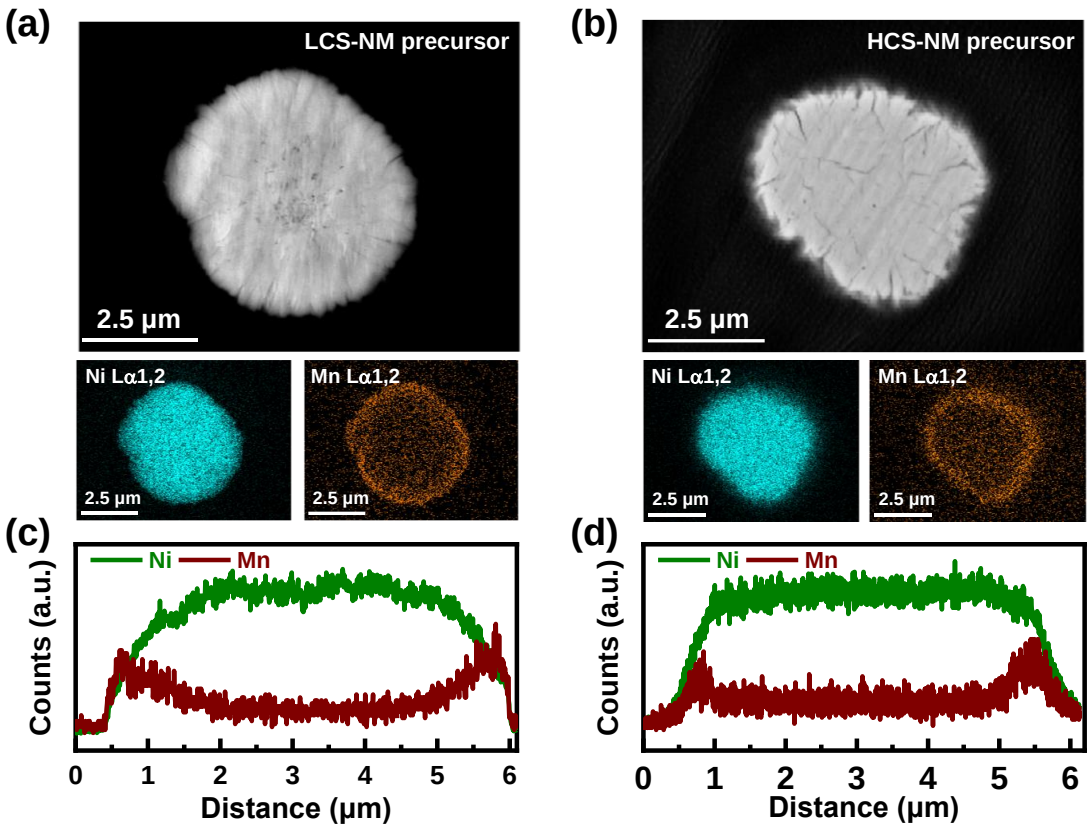

Fig. S2 Cross-sectional SEM images and corresponding EDS elemental maps of Ni and Mn for the (a) LCS-NM precursor and (b) HCS-NM precursor. EDS line scan profiles of the (c) LCS-NM precursor and (d) HCS-NM precursor.

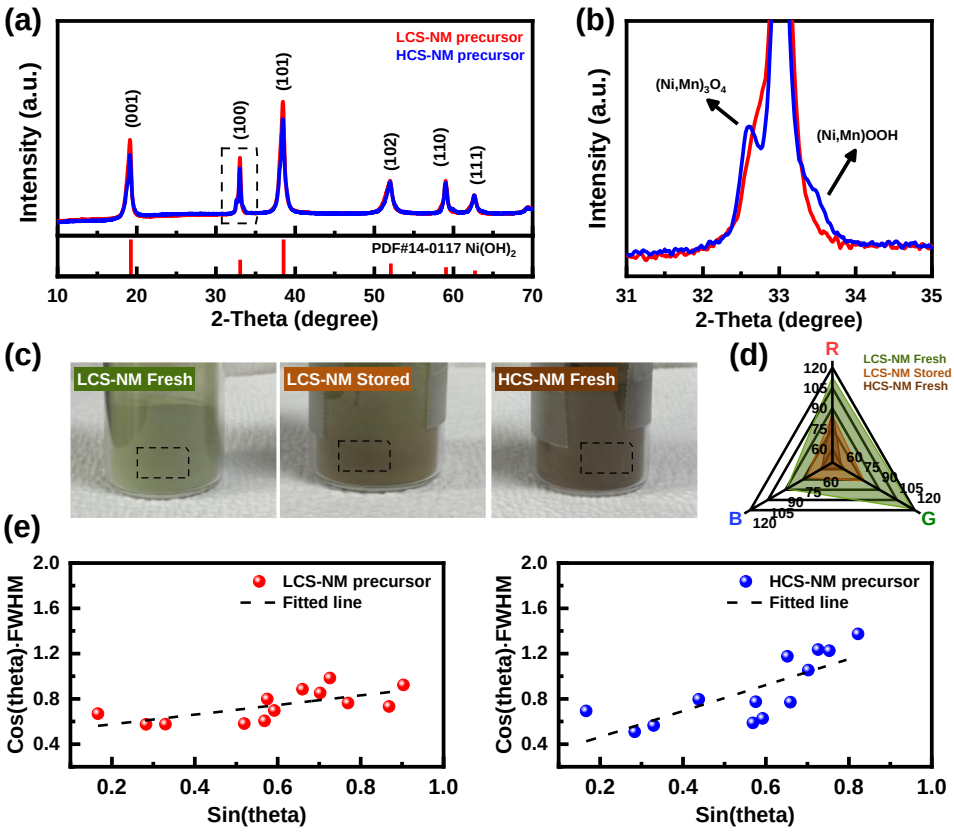

Fig. S3 (a) XRD patterns of LCS-NM and HCS-NM precursor powders. (b) Magnified diffractograms highlighting the incorporation of the oxyhydroxide phase in the HCS-NM precursor. (c) Photographs of each precursor (fresh LCS-NM, stored LCS-NM, and HCS-NM) and (d) RGB codes extracted from the dashed boxes in (c). (e) Corresponding Williamson–Hall plots derived from the XRD patterns.

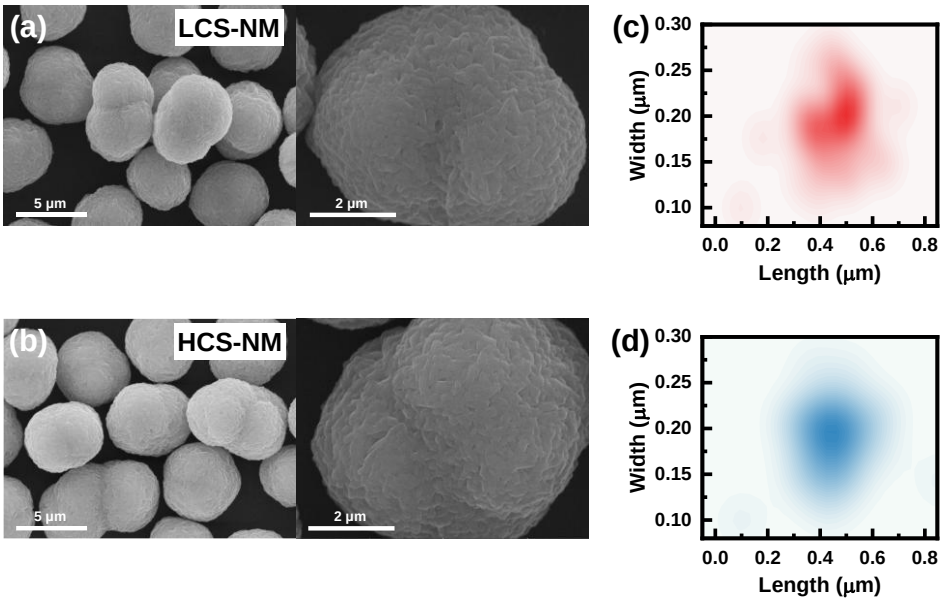

Fig. S4 SEM images of (a) LCS-NM and (b) HCS-NM. 2D kernel density plots illustrating the length and width distribution of primary particles for (c) LCS-NM and (d) HCS-NM.

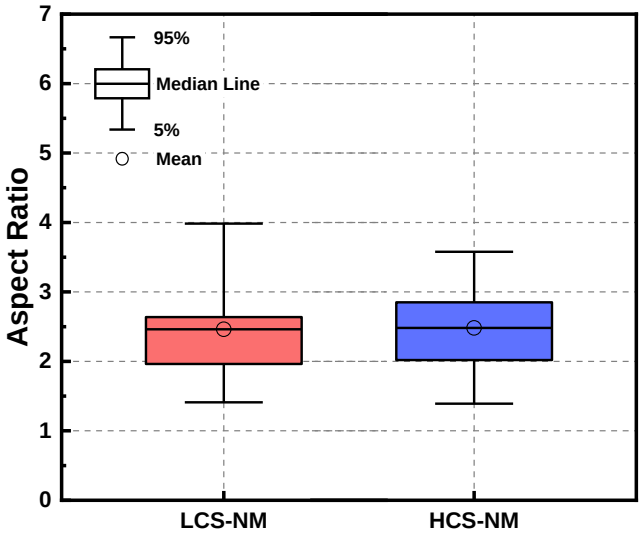

Fig. S5 Box-and-whisker plots displaying the aspect ratios (length/width) calculated from SEM images of LCS-NM and HCS-NM.

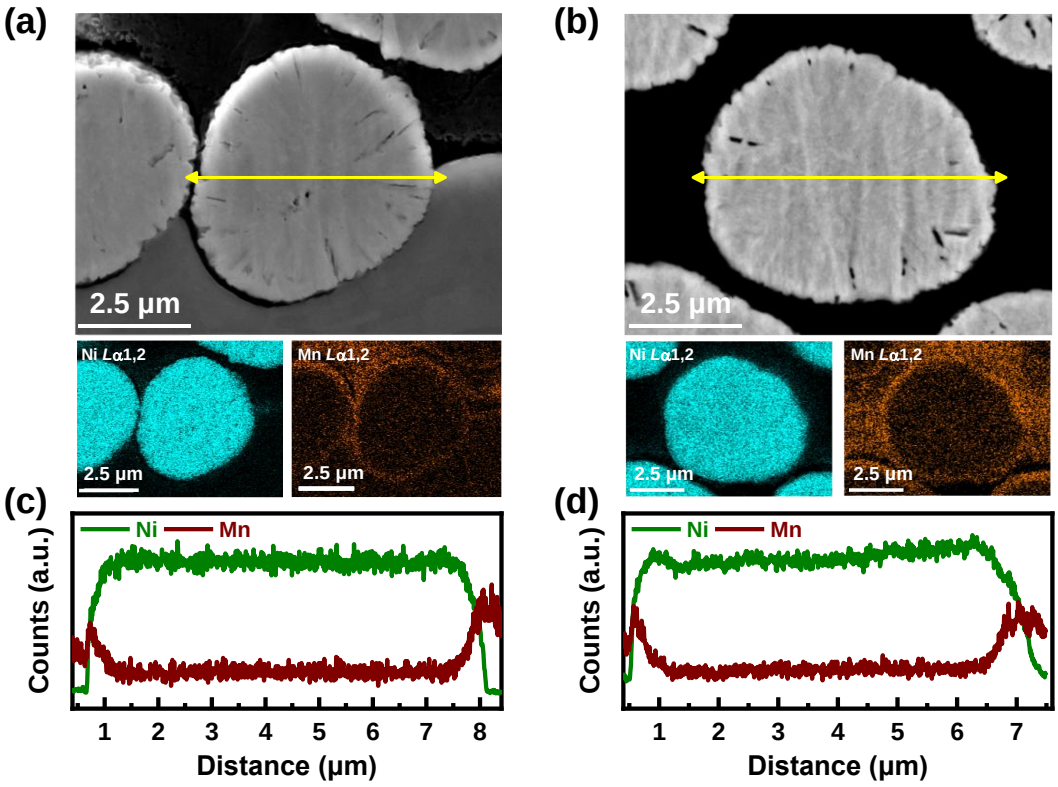

Fig. S6 Cross-sectional SEM images and corresponding EDS elemental maps of Ni and Mn for (a) LCS-NM and (b) HCS-NM. EDS line scan profiles of (c) LCS-NM and (d) HCS-NM.

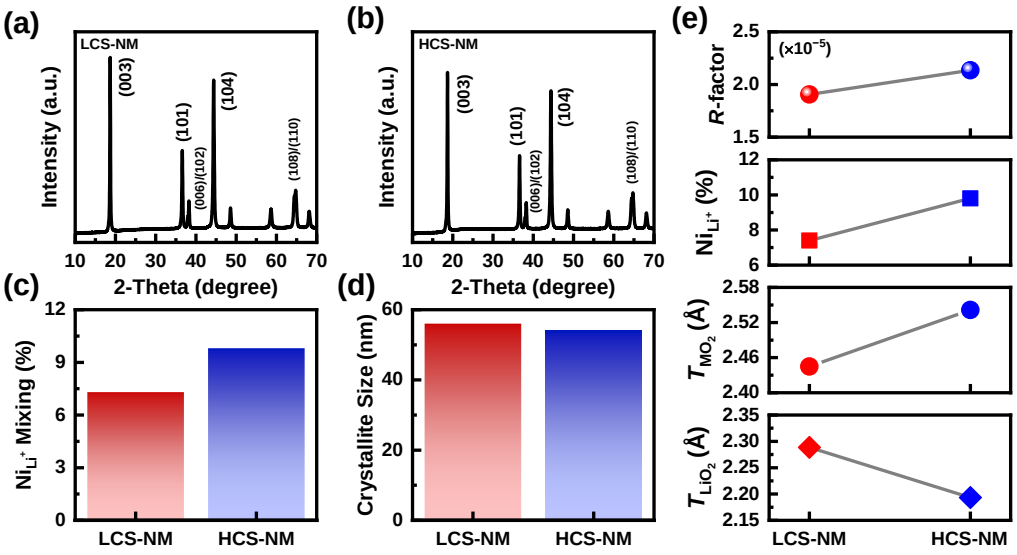

Fig. S7 XRD pattern of (a) LCS-NM and (b) HCS-NM. Calculated value of (c) Ni/Li mixing and (d) crystallite size of each sample. (e) Calculated *R* factor[a)] and thickness of transition metal slab (T_{MO_2})[b)] and lithium slab (T_{LiO_2})[c)].

a) *R* factor = $[I_{(006)}/I_{(102)}]/I_{(101)}$

b) $T_{MO_2}=2(1/3-Z_{ox}^{*})\cdot c_{lattice}$

c) $T_{LiO_2}=(c_{lattice}/3)- T_{MO_2}$

* Z_{ox} = Wcykoff position of oxygen

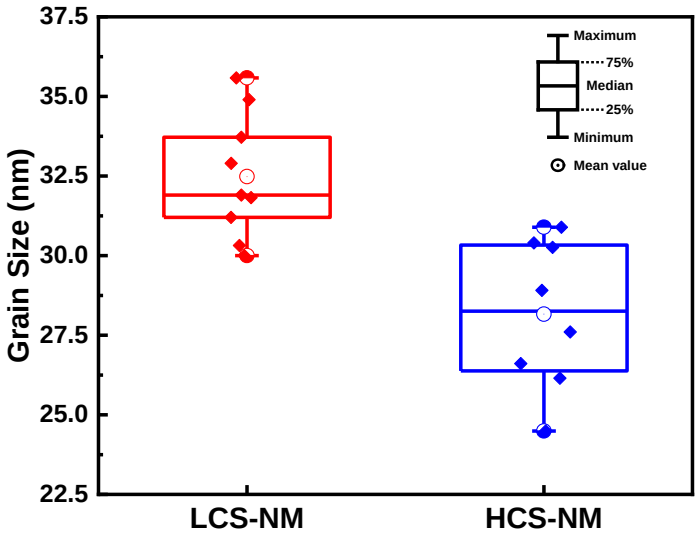

Fig. S8 Box-and-whisker plots displaying the grain sizes of LCS-NM and HCS-NM obtained from multiple XRD measurements.

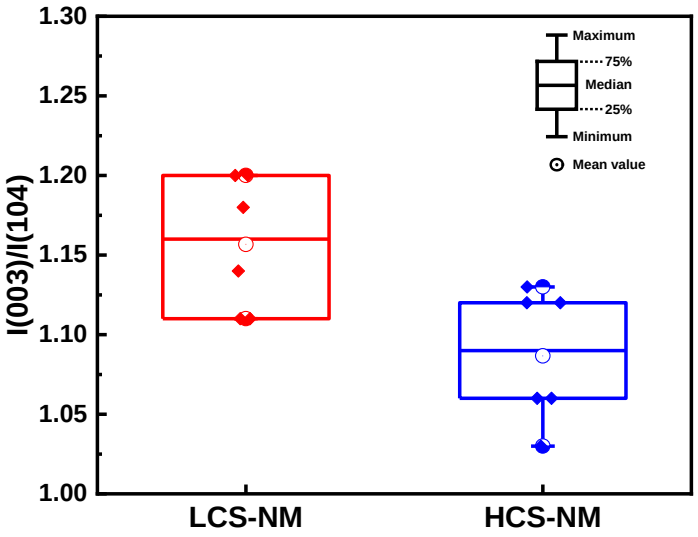

Fig. S9 Box-and-whisker plots displaying the peak intensity ratios of the (003) to (104) planes for LCS-NM and HCS-NM, obtained from multiple XRD measurements.

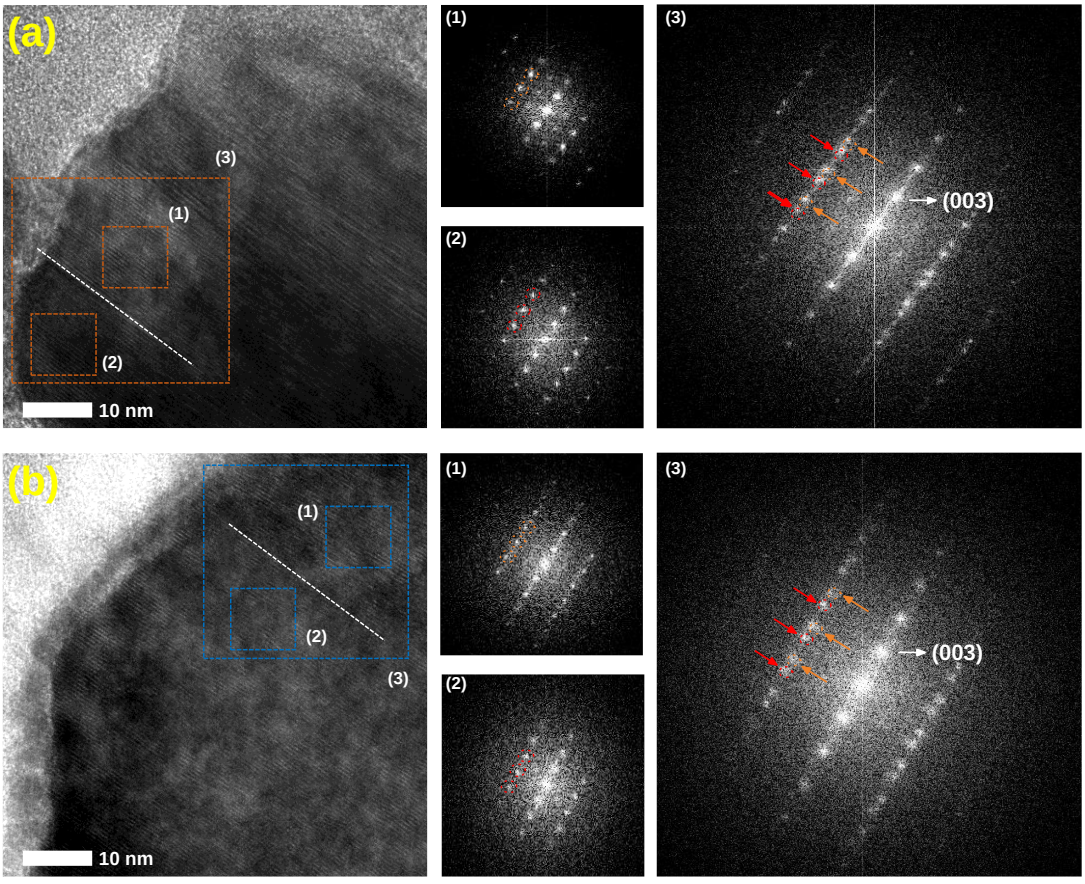

Fig. S10 HRTEM images of (a) LCS-NM and (b) HCS-NM, along with FFT patterns for selected regions. Region 3 encompasses both Regions 1 and 2, revealing twinned defects existing between mirror planes (indicated by the white dashed line). The red and orange arrows in Region 3 correspond to the electron diffraction patterns of the (101), (102), and (104) planes from selected Regions 1 and 2, respectively.

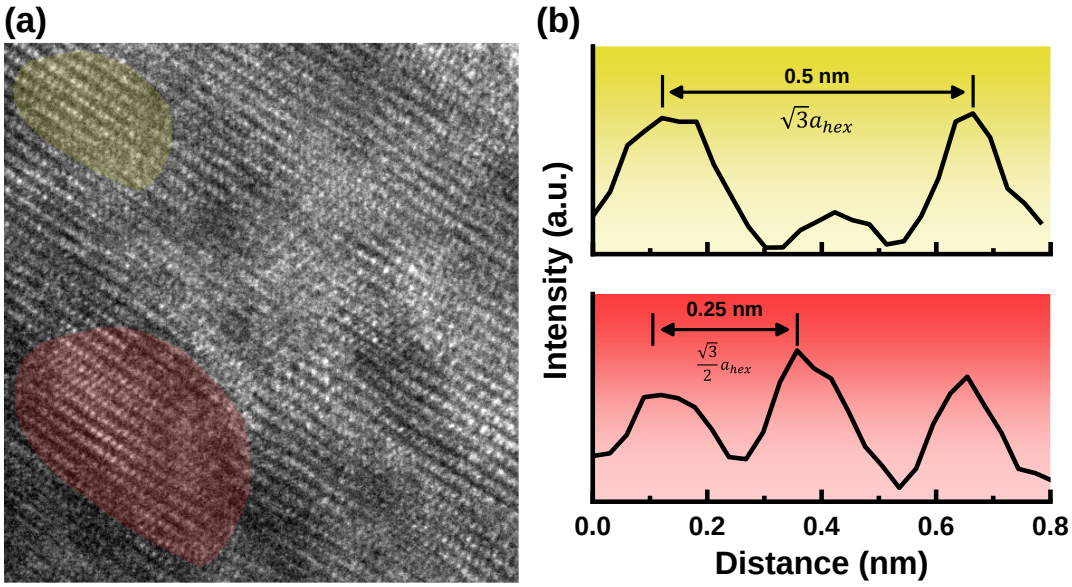

Fig. S11 (a) HRTEM image of LCS-NM and (b) corresponding line profiles for each region. Two randomly selected regions confirm the random distribution of the super-lattice (Li/TM disordered structure, yellow region) with a $\sqrt{3}a_{hex}$ unit normal layered structure (red region) with a $\frac{\sqrt{3}}{2}a_{hex}$ unit.

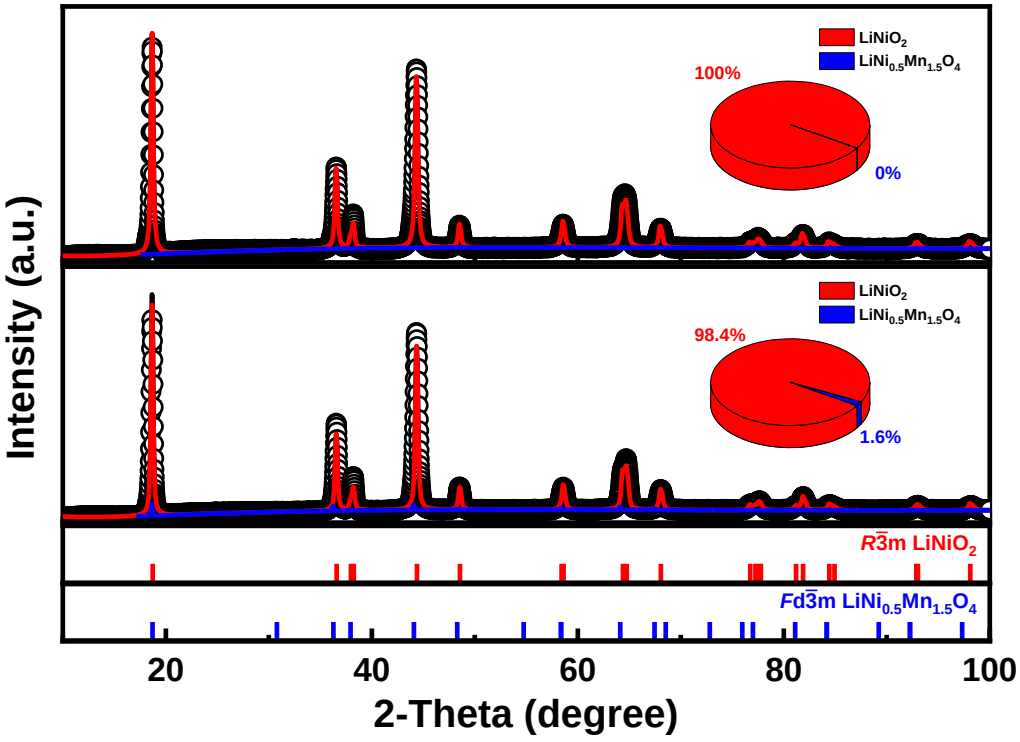

Fig. S12 Relative phase compositions of the layered ($R\bar{3}m$) and spinel ($Fd\bar{3}m$) phases determined via Rietveld refinement analysis. The inset pie charts illustrate the relative fractions of the layered and spinel phases.

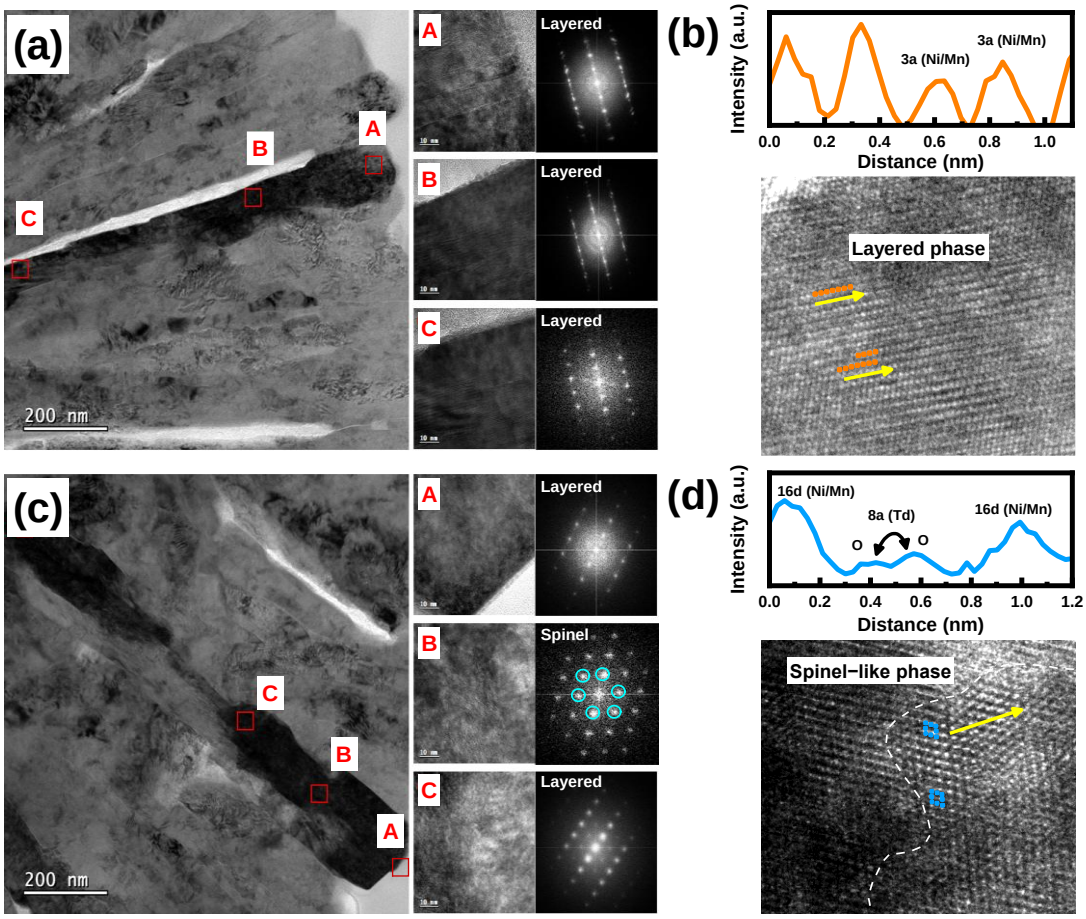

Fig. S13 HRTEM images and FFT patterns of selected areas for (a) LCS-NM and (c) HCS-NM. Corresponding line profile analyses of the (b) layered structure and (d) spinel structure domains.

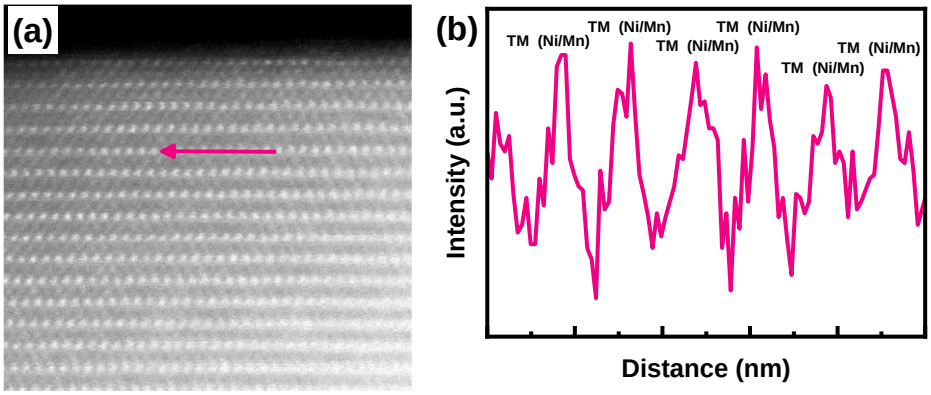

Fig. S14 (a) Enlarged STEM-HAADF image of LCS-NM and (b) line profile spectra along the pink arrow shown in (a).

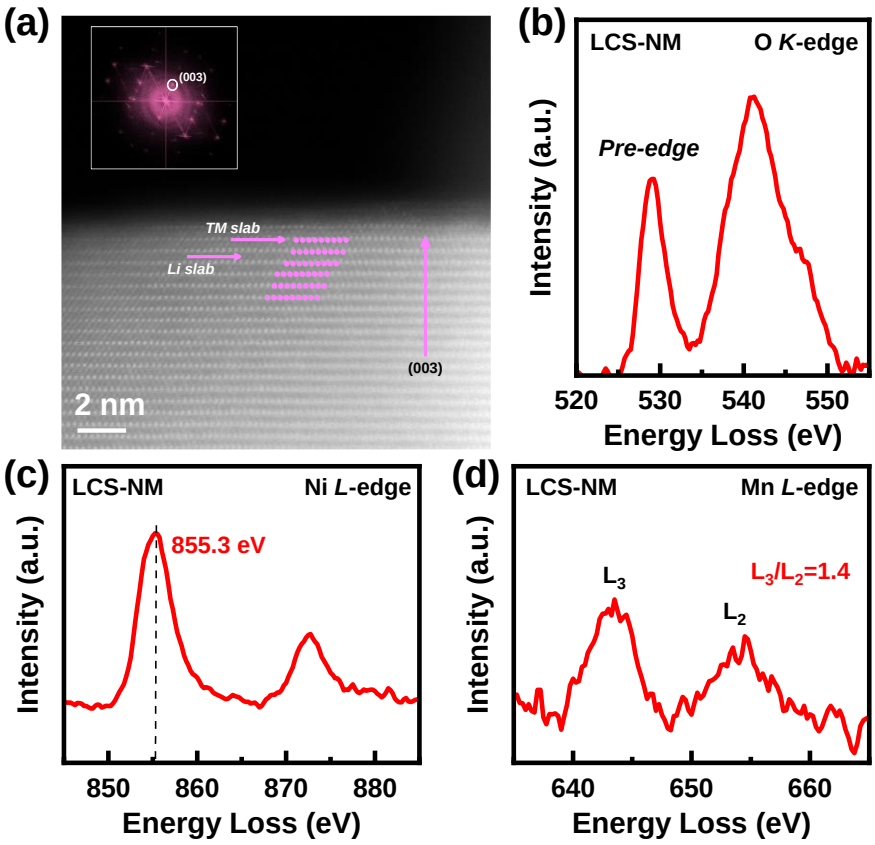

Fig. S15 (a) STEM-HAADF image of LCS-NM (inset: SAED pattern). Corresponding EELS spectra for the (b) O *K*-edge, (c) Ni *L*-edge, and (d) Mn *L*-edge.

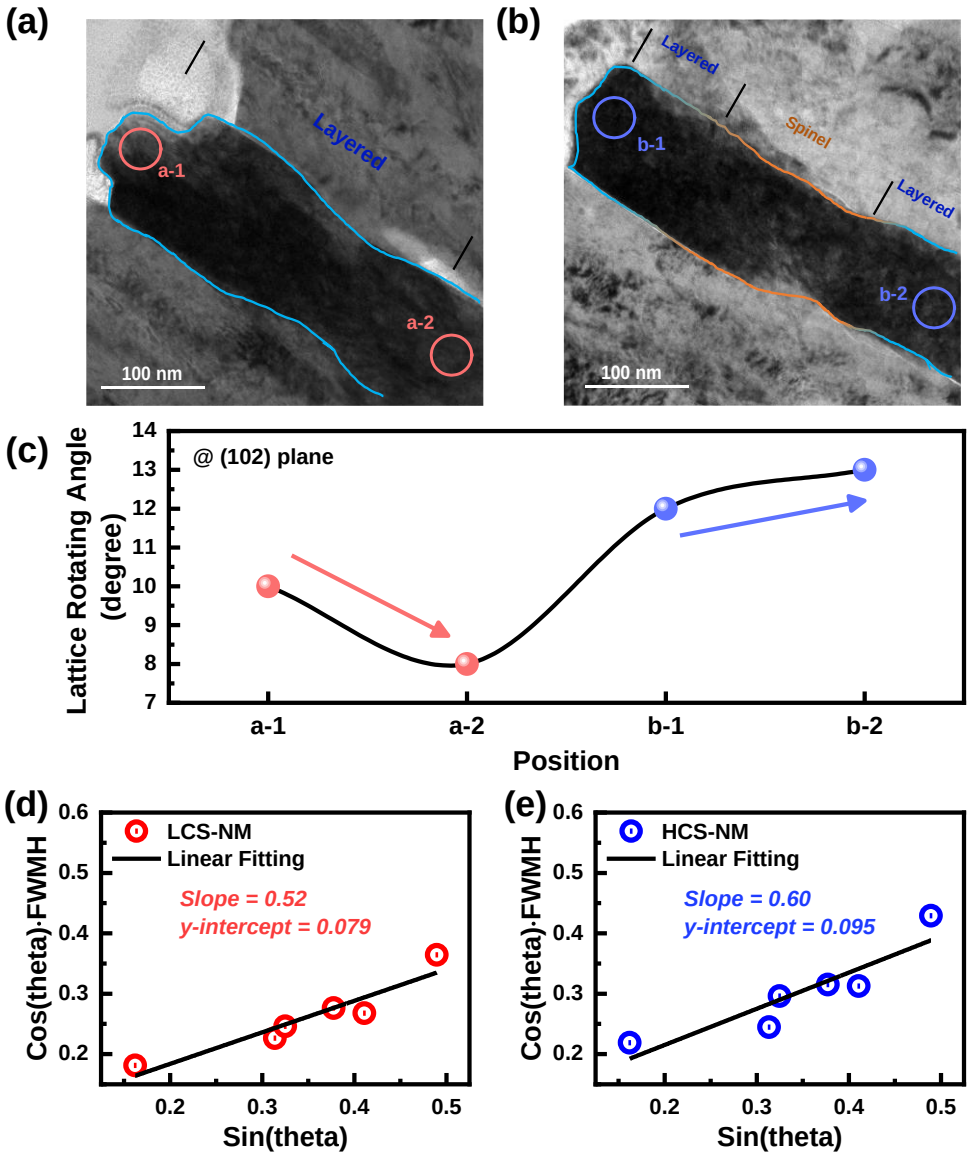

Fig. S16 HRTEM images of (a) LCS-NM and (b) HCS-NM. (c) Calculated in-plane lattice rotation angles in the layered structure for each region. The rotation angles were derived from selected regions (a-1, a-2 for LCS-NM; b-1, b-2 for HCS-NM). Williamson–Hall plots for (d) LCS-NM and (e) HCS-NM extracted from XRD results.

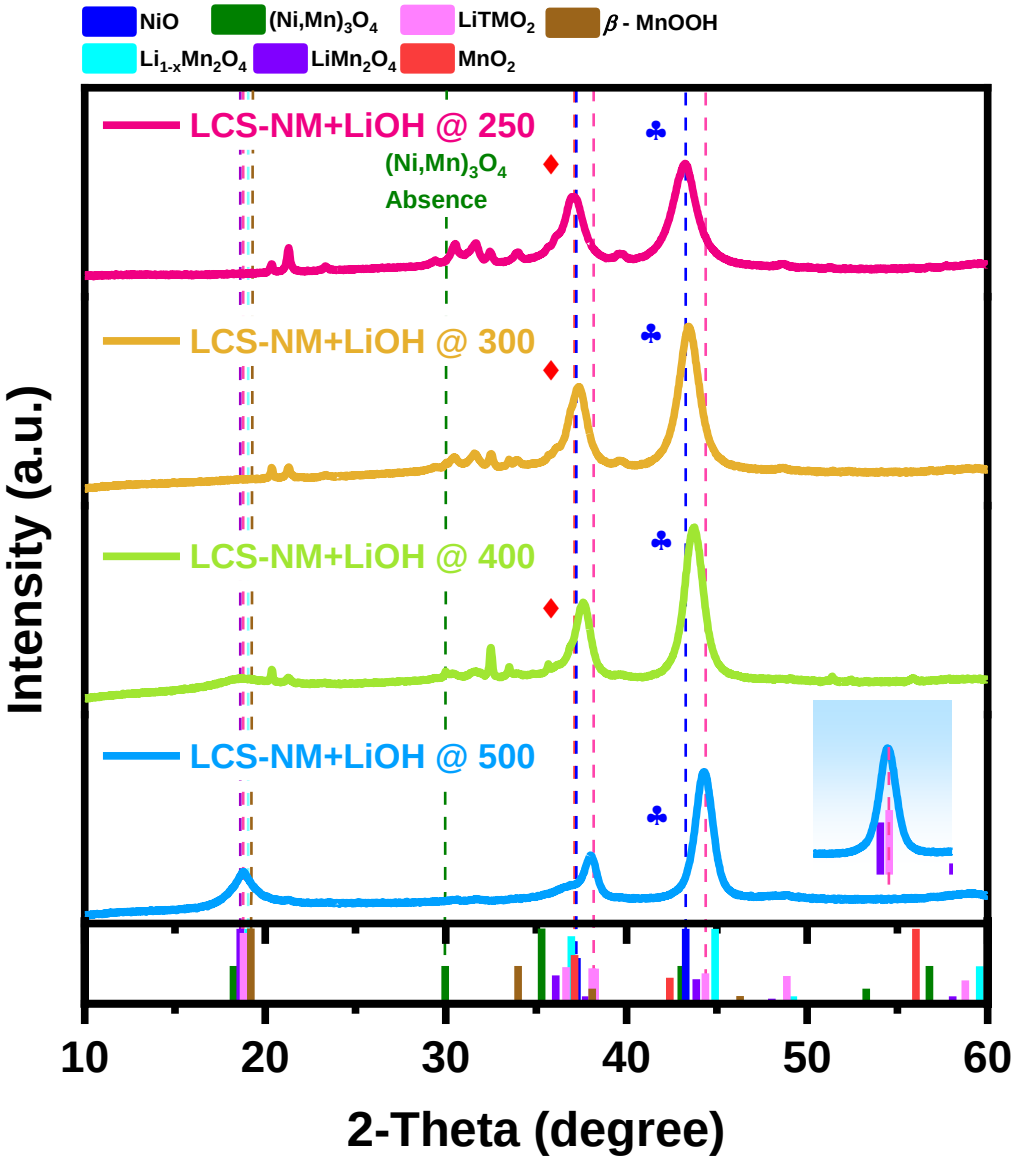

Fig. S17 Ex situ XRD patterns of the mixture of LCS-NM precursor and $LiOH \cdot H_2O$ lithiated at 250, 300, 400, and 500 °C. Red diamonds, blue clovers, and pink notes denote MnO_2, NiO, and layered $LiTMO_2$ phases, respectively.

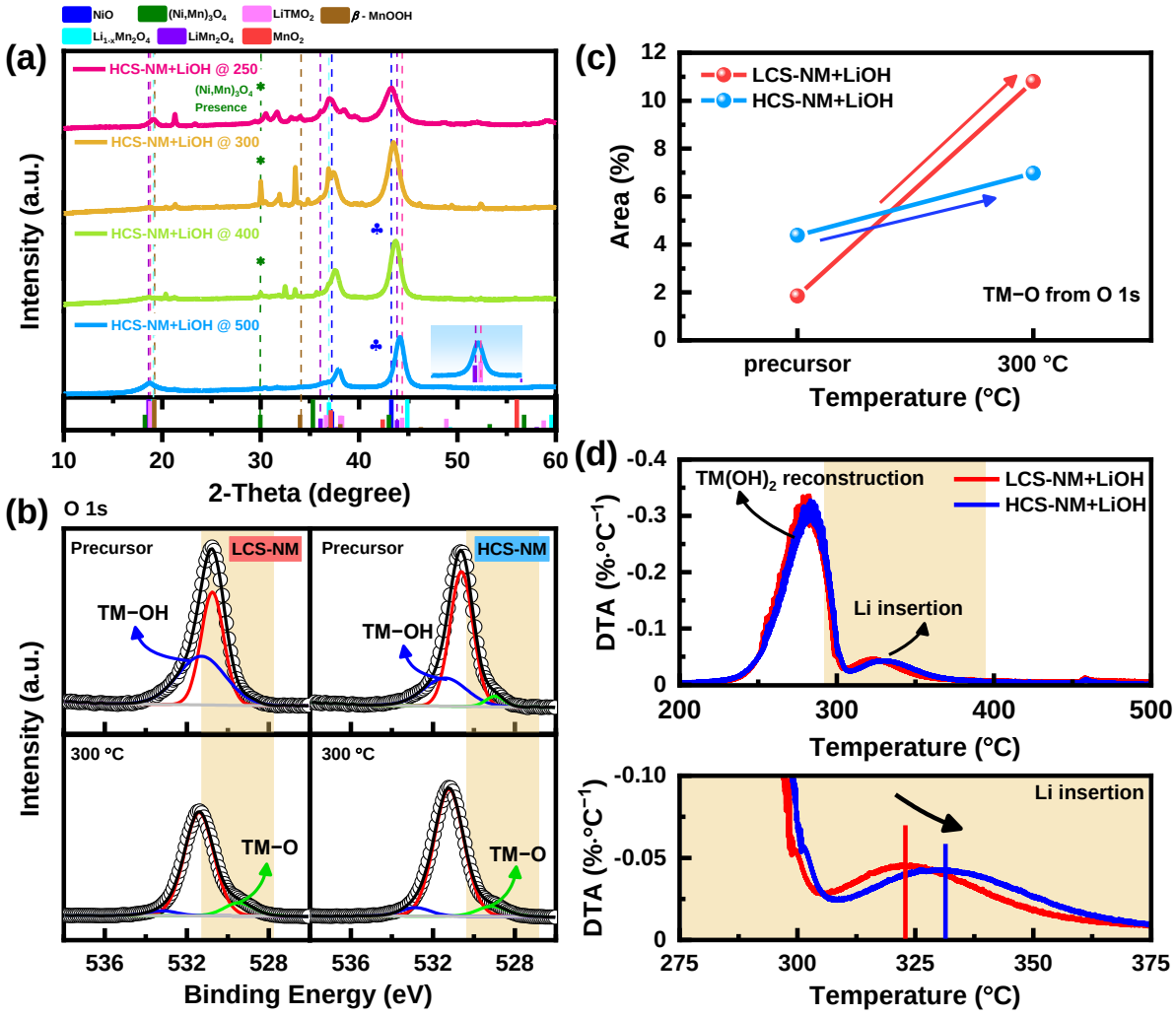

Fig. S18 (a) Ex situ XRD patterns of the mixture of HCS-NM precursor and $LiOH{\cdot}H_2O$ lithiated at 250, 300, 400, and 500 °C. Green asterisks, blue clovers, and pink notes denote spinel TM_3O_4, NiO, and layered $LiTMO_2$ phases, respectively. (b) O 1s XPS spectra of LCS-NM and HCS-NM mixtures at the precursor stage and after heating to 300 °C, with (c) corresponding fitted areas for M–O binding. (d) DTA curves derived from TGA during heating from RT to 500 °C for mixtures of LCS-NM/HCS-NM precursors and LiOH.

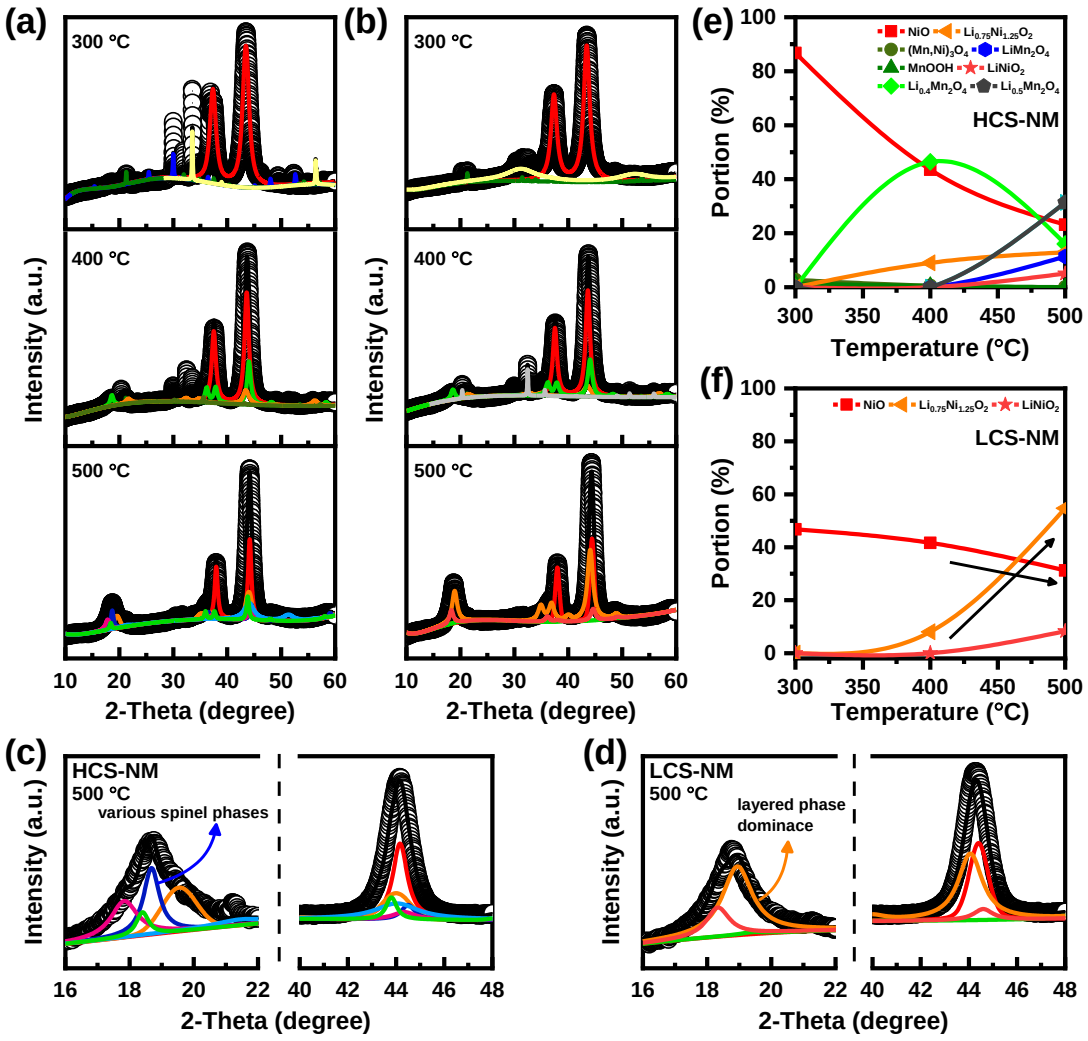

Fig. S19 Rietveld refinement patterns of samples quenched at 300, 400, and 500 °C for (a) HCS-NM + LiOH and (b) LCS-NM + LiOH. Magnified diffractograms at 500 °C for (c) HCS-NM + LiOH and (d) LCS-NM + LiOH. Changes in the relative fractions of fitted crystal phases during heat treatment for (e) HCS-NM + LiOH and (f) LCS-NM + LiOH. *Note:* Rietveld refinement quantitatively confirms the presence of various spinel intermediates in the HCS-NM precursor (e.g., $(Ni,Mn)_3O_4$, $Li_{0.4}TM_2O_4$, and $Li_{0.5}TM_2O_4$), with a significant increase in Li-inserted spinel content between 400 and 500 °C. Notably, HCS-NM exhibits nearly twice the content of the lithiated spinel phase (e.g., $Li_{0.5}Mn_2O_4$) compared to the layered phase even at 500 °C, suggesting an unfavorable phase transformation from spinel to layered structures during high-temperature heating. In contrast, the LCS-NM precursor predominantly transitions to layered structures (e.g., $Li_{0.75}Ni_{1.25}O_2$ and $LiNiO_2$) without significant intermediates. At 500 °C, approximately 60% of the partially lithiated layered structure (e.g., $Li_{0.75}NiO_2$) is detected in LCS-NM, accompanied by a decrease in the NiO rock-salt phase, suggesting direct Li incorporation into NiO.

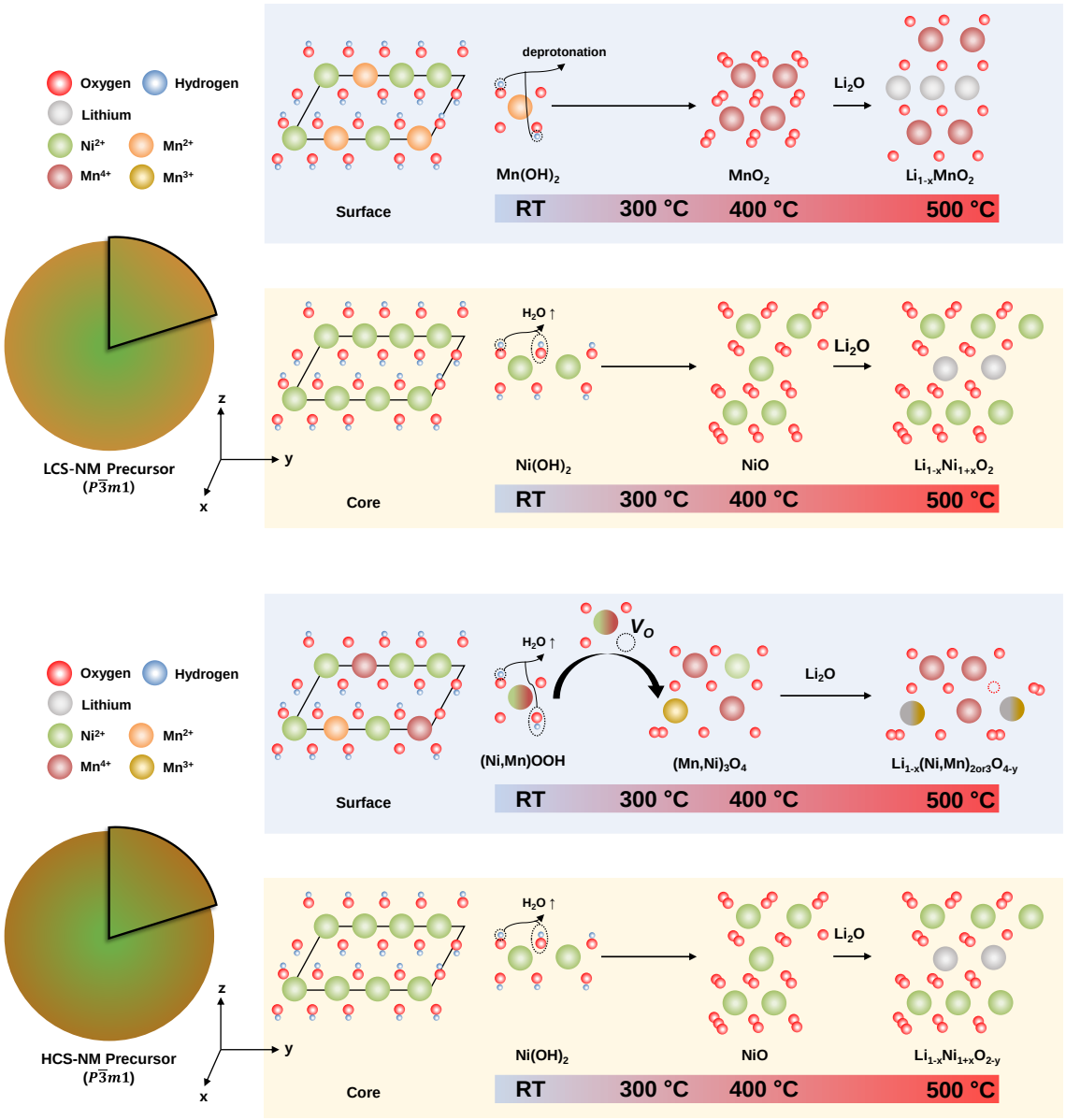

Fig. S20 Schematic illustration of the solid-state reaction mechanism for each precursor. While the normal core/shell precursor follows the archetypal phase evolution mechanism, the oxidized Mn in the HCS-NM shell exhibits distinct surface properties. This deviation is attributed to the formation of intermediates starting from $(Ni,Mn)_3O_4$, which are not observed in the conventional mechanism.

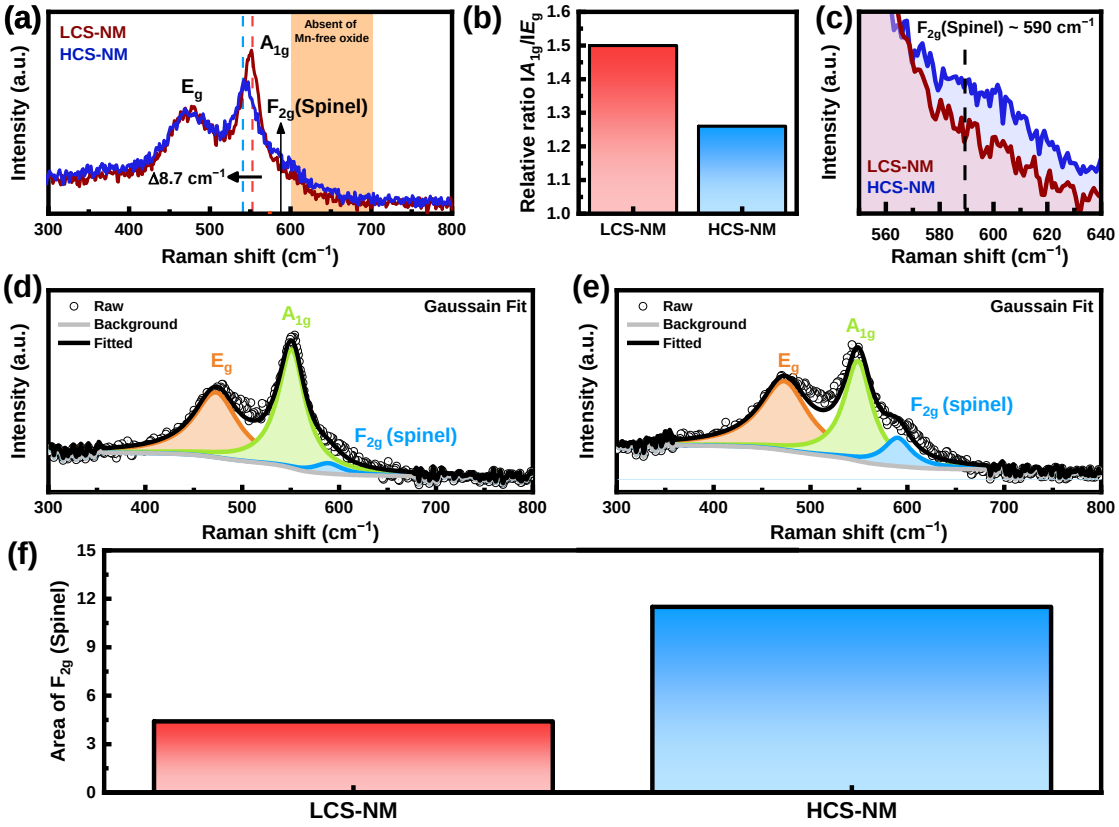

Fig. S21 (a) Raman spectra of LCS-NM and HCS-NM acquired using a 532 nm laser. (b) Relative A_{1g}/E_g mode ratio of the layered structure and (c) F_{2g} mode from the spinel structure. Gaussian fitting results of the Raman spectra for (d) LCS-NM and (e) HCS-NM. (f) Relative fraction of the F_{2g} mode (spinel structure) obtained via Gaussian fitting.

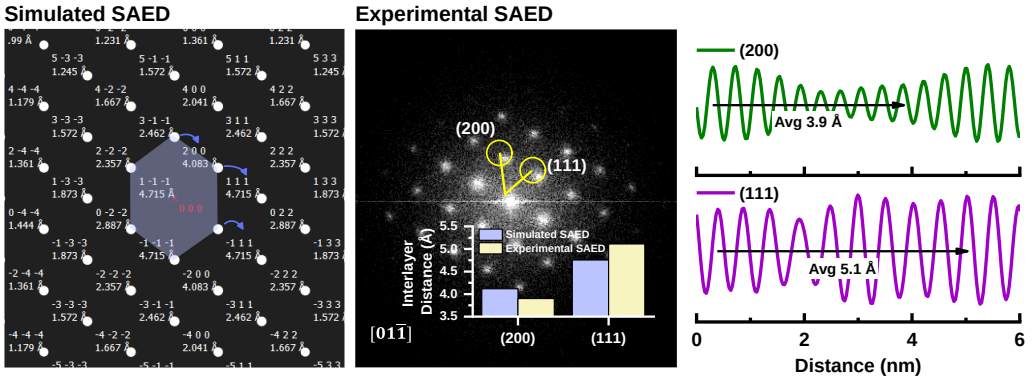

Fig. S22 Simulated SAED pattern of the spinel cathode along the [01$\bar{1}$] projection and the experimental SAED pattern obtained from the HCS-NM spinel phase. Corresponding line profiles along the (200) and (111) lattice planes.

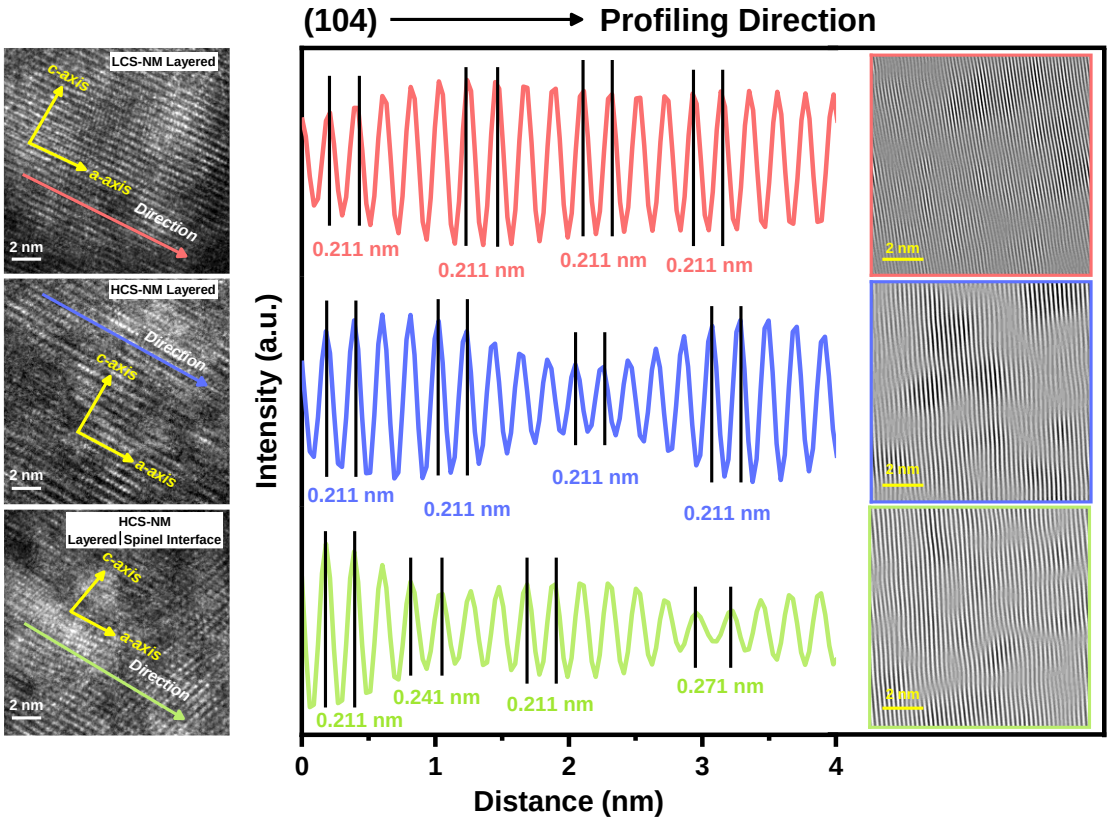

Fig. S23 HRTEM images of LCS-NM and HCS-NM showing regions of coexisting layered or layered-spinel phases. Line profiles along the (104) lattice plane for selected areas in LCS-NM (red arrow) and HCS-NM (blue and green arrows). Yellow arrows in the HRTEM images indicate the axis direction based on the hexagonal unit cell. The red and blue plots correspond to the layered structure of LCS-NM and HCS-NM, respectively, while the green plot is extracted from the layered/spinel interface of the HCS-NM structure. All line profiles and lattice distances were extracted from IFFT images (right) along the selected directions.

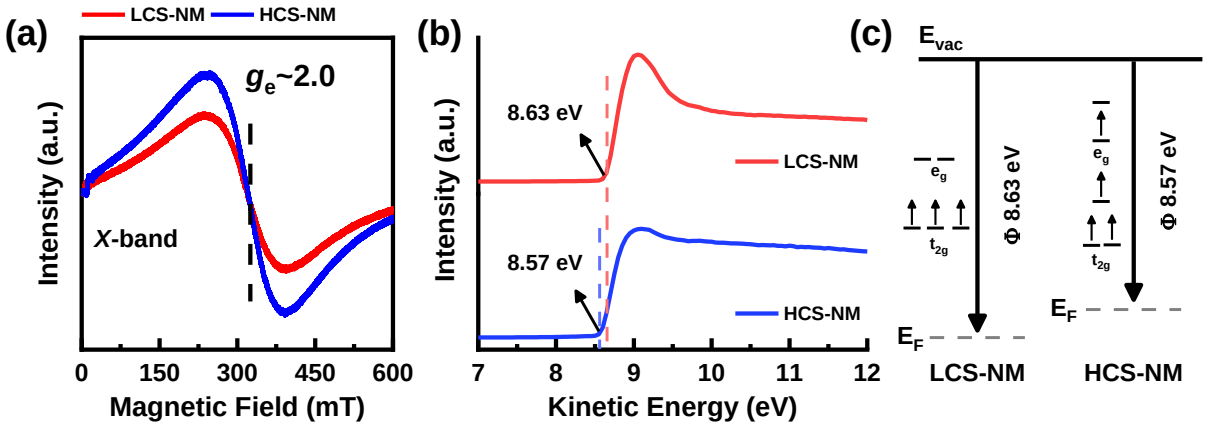

Fig. S24 (a) X-band EPR spectra of LCS-NM and HCS-NM. (b) UPS spectra of LCS-NM and HCS-NM used to determine the work function (Φ). (c) Schematic representation of the change in work function and electron configuration between $Mn^{4+}(t_{2g}^3)$ and $Mn^{3+}(t_{2g}^3 e_g^1)$ with increasing Fermi level.

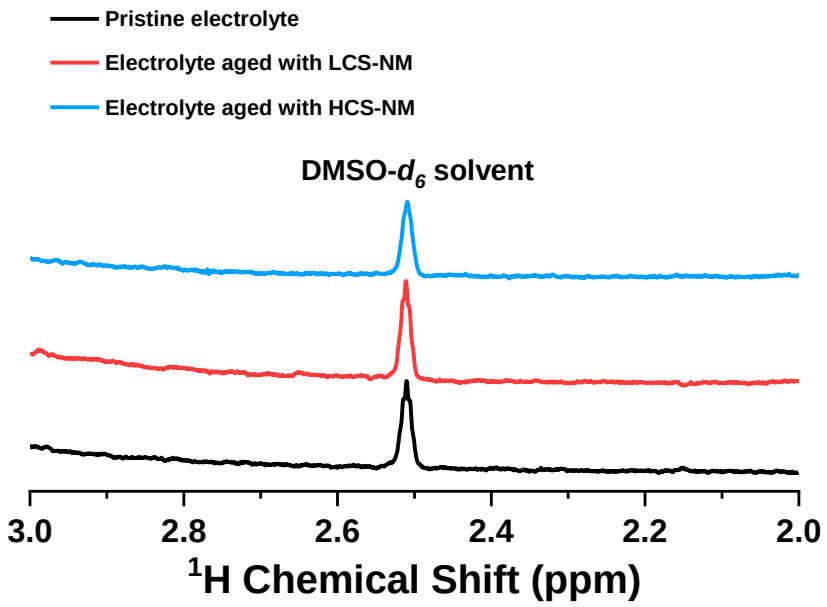

Fig. S25 ^{1}H NMR spectra of the DMSO-d_6 solvent with three different electrolytes. The solvent peaks exhibit identical positions, indicating no interaction between the samples and the solvent during the NMR sampling procedure.

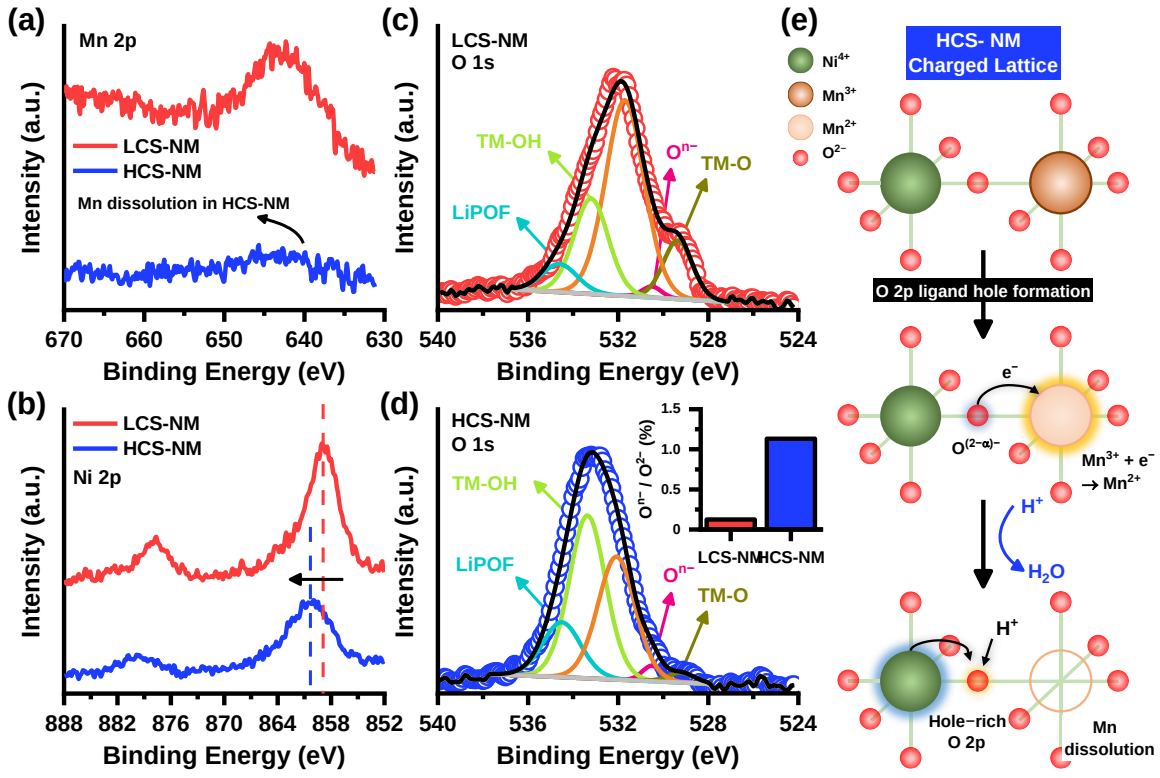

Fig. S26 (a, b) XPS spectra of the (a) Mn 2p and (b) Ni 2p regions obtained from thermally aged LCS-NM and HCS-NM cathodes. (c, d) O 1s spectra of (c) LCS-NM and (d) HCS-NM. The inset in (d) displays the ratio of oxidized oxygen species (O^{n-}) to lattice oxygen (O^{2-}). (e) Schematic illustration of the disproportionation mechanism induced by JT active Mn, facilitated by electron exchange involving O 2p ligand holes.

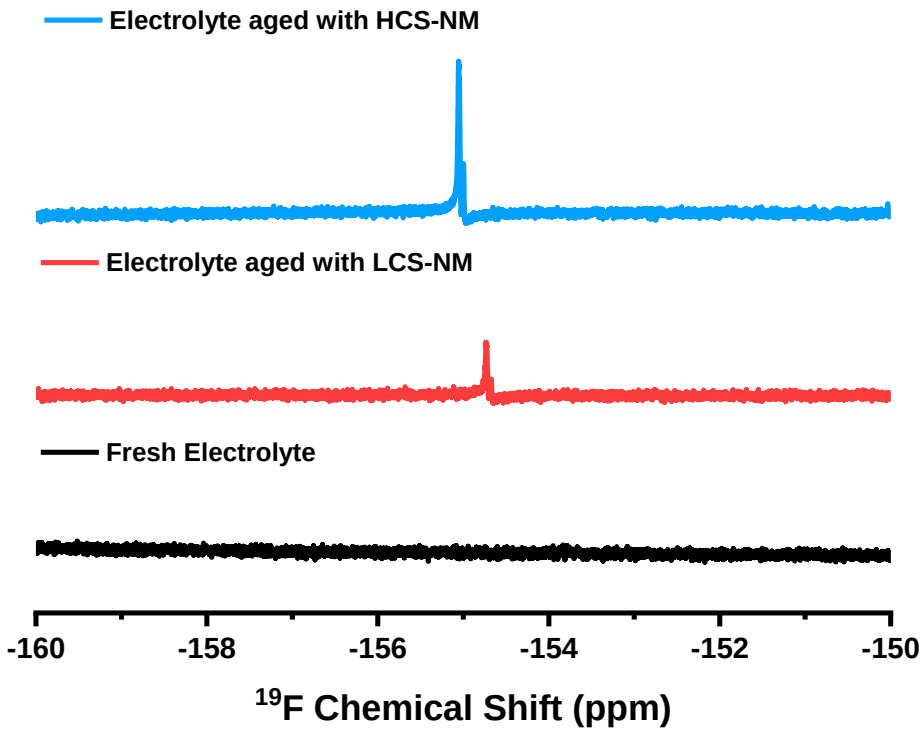

Fig. S27 ^{19}F NMR spectra obtained with three different electrolytes. The peaks near –155 ppm correspond to hydrolyzed fluoride species (F^-). The electrolyte aged with the HCS-NM cathode exhibits the sharpest and most intense F^- peak.

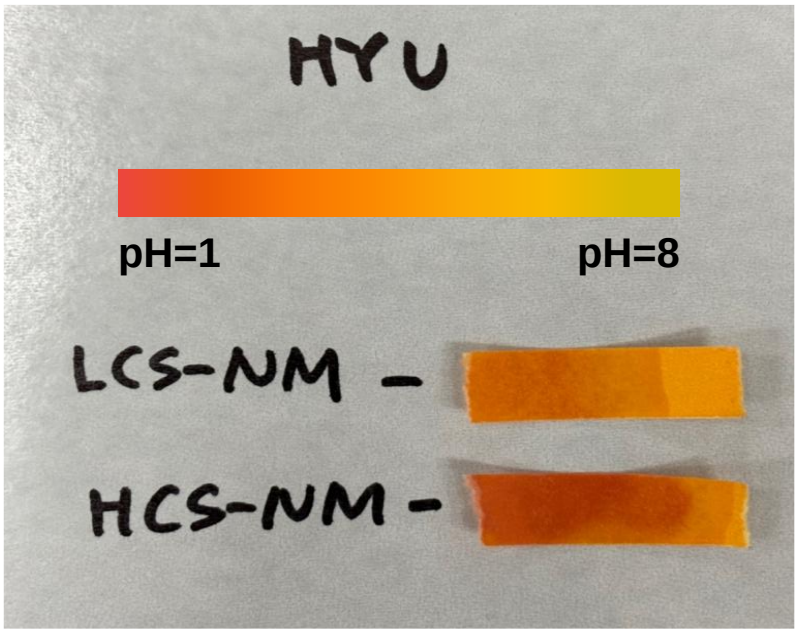

Fig. S28 Photographs of pH paper after immersion in each thermally aged electrolyte.

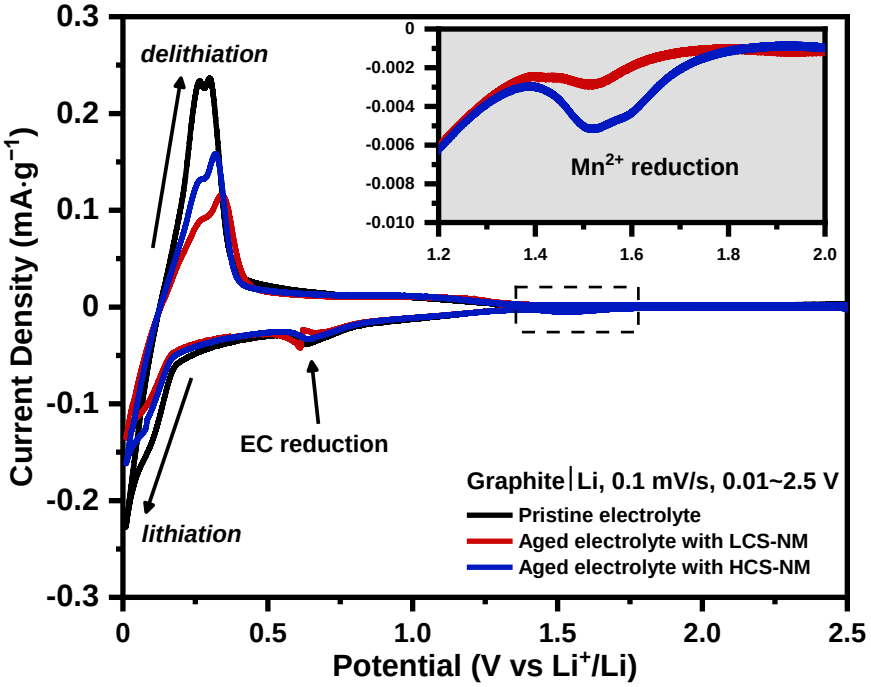

Fig. S29 Cyclic voltammetry curves of Graphite/Li half-cells filled with electrolytes aged with LCS-NM and HCS-NM cathodes.

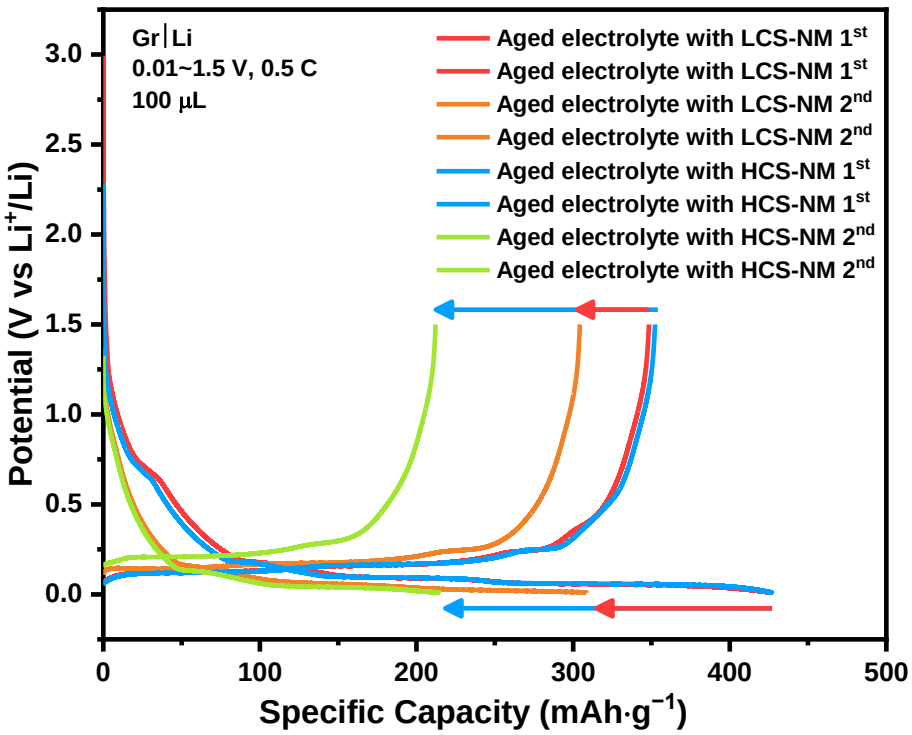

Fig. S30 Charge/discharge curves for the 1st and 2nd cycles of Graphite/Li half-cells using electrolytes aged with LCS-NM and HCS-NM cathodes. The cell using the HCS-NM-aged electrolyte shows significantly larger initial capacity loss in the second cycle.

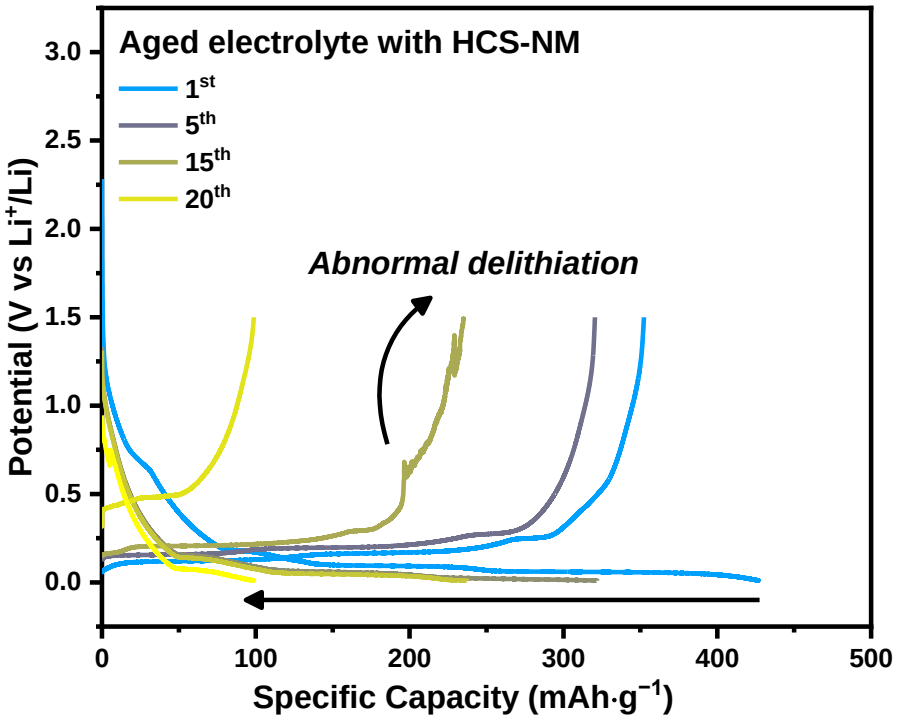

Fig. S31 Charge/discharge curves of Graphite/Li half-cell cycling using the electrolyte aged with the HCS-NM cathode.

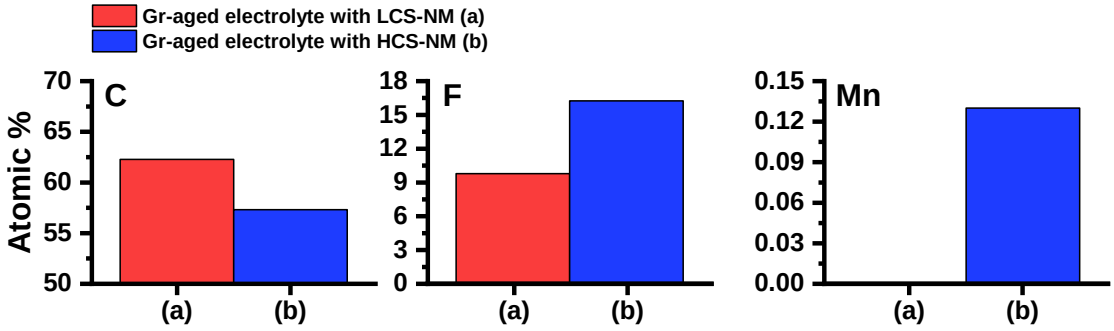

Fig. S32 Atomic percentages of C, F, and Mn obtained from EDS analysis of the cycled graphite anode using each aged electrolyte.

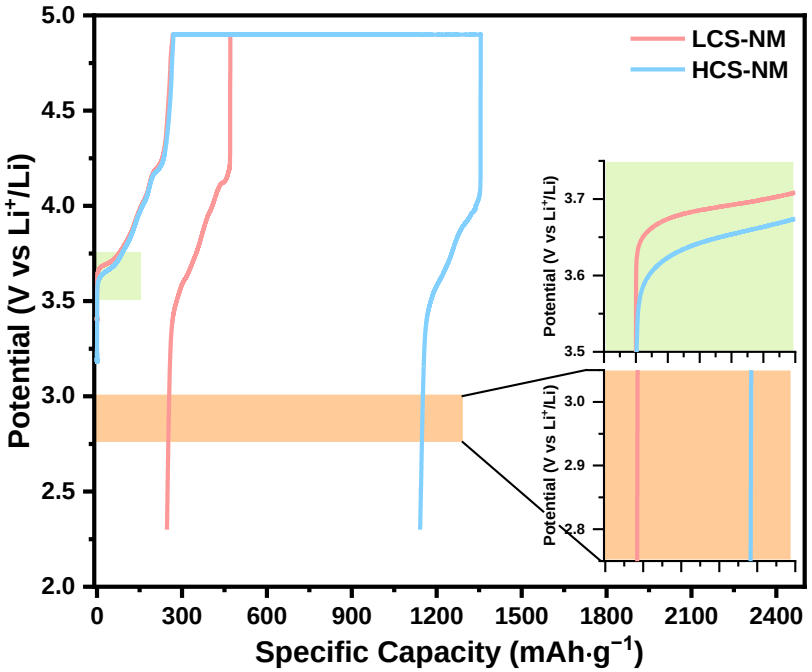

Fig. S33 Charge/discharge curves of the initial cycle at 0.1 C (2.3–4.9 V) for LCS-NM and HCS-NM. Green and orange boxes indicate the initial redox potential for the layered structure and the potential range for further lithiation of the spinel phase (from stoichiometric Li:TM=1:2 to Li-rich Li:TM=1:1), respectively. *Note:* Half-cells assembled with each cathode were cycled over a wide potential range (2.3–4.9 V vs. Li^+/Li) to investigate additional Li (de)lithiation reactions. Despite the coexistence of the $LiTM_2O_4$ spinel-like phase in HCS-NM, an extra two-phase reaction (plateau) corresponding to further Mn redox was not observed. However, the HCS-NM exhibited a constant voltage (CV) charging period almost four times longer than that of LCS-NM. This implies that the unstable chemical state of surface Mn in HCS-NM promotes parasitic reactions with the electrolyte, increasing irreversible lithium consumption and significantly retarding delithiation kinetics, thereby extending the CV period even at identical high-voltage cutoffs.

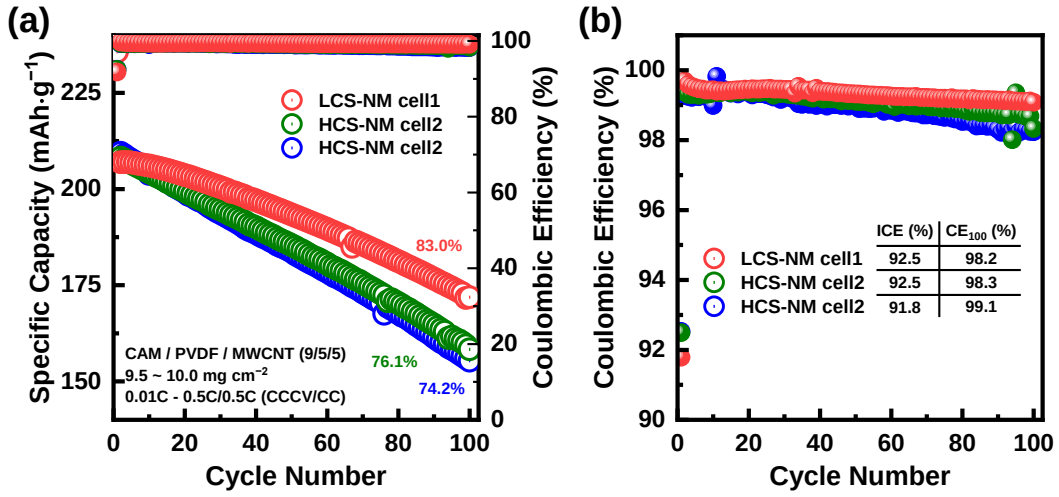

Fig. S34 (a) Long-term cycling performance of high-loading LCS-NM and HCS-NM. (b) Coulombic efficiencies during the long-term test.

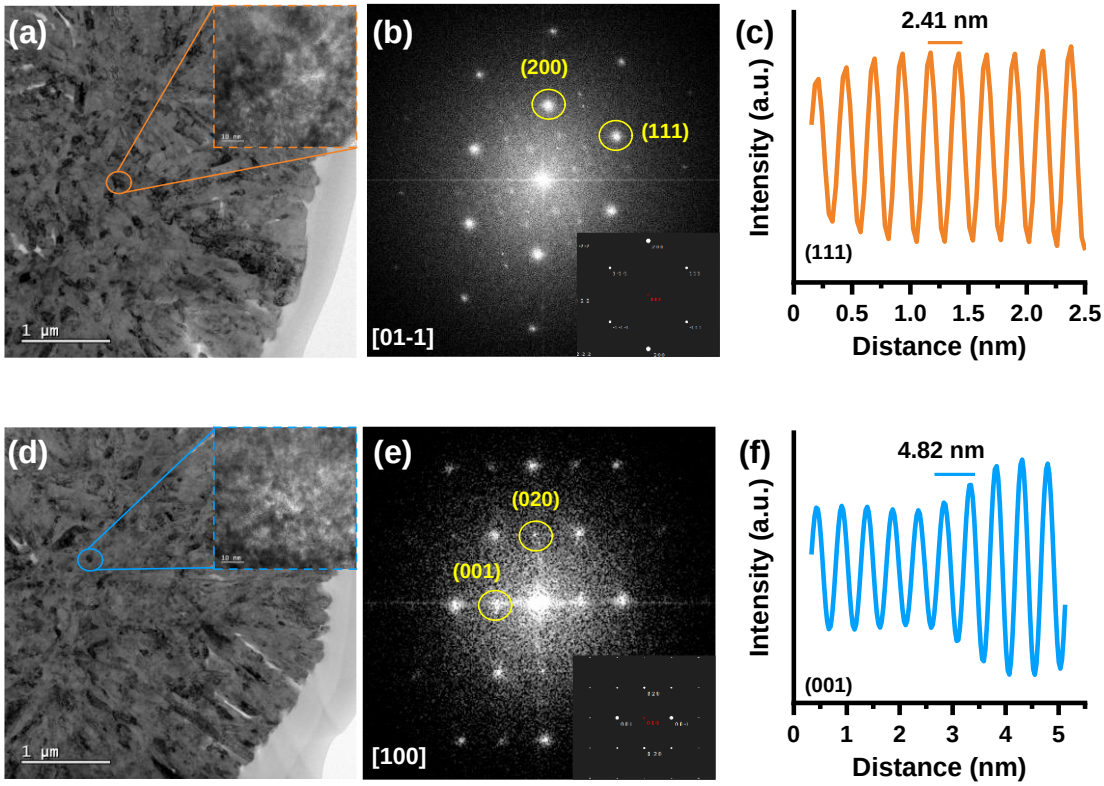

Fig. S35 HRTEM images, corresponding SAED patterns, and line profiles along the (111) and (001) planes of primary particles located in the core regions of (a–c) LCS-NM and (d–f) HCS-NM cathodes. The insets in the SAED patterns display the simulated electron diffraction patterns of the rock-salt and monoclinic phases.

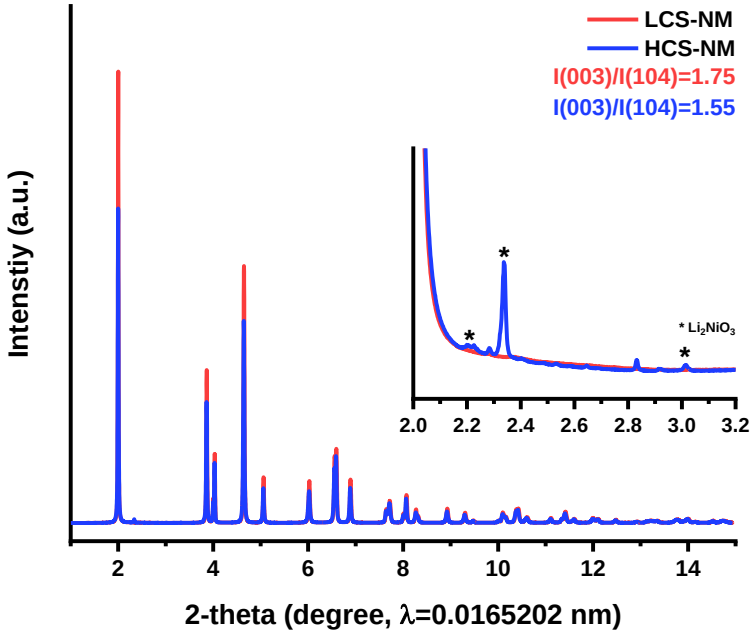

Fig. S36 Synchrotron XRD patterns of the LCS-NM and HCS-NM cathodes. The inset shows magnified diffractograms, highlighting the presence of the Li-rich layered oxide (Li_2NiO_3, *C*2/*m*) phase.

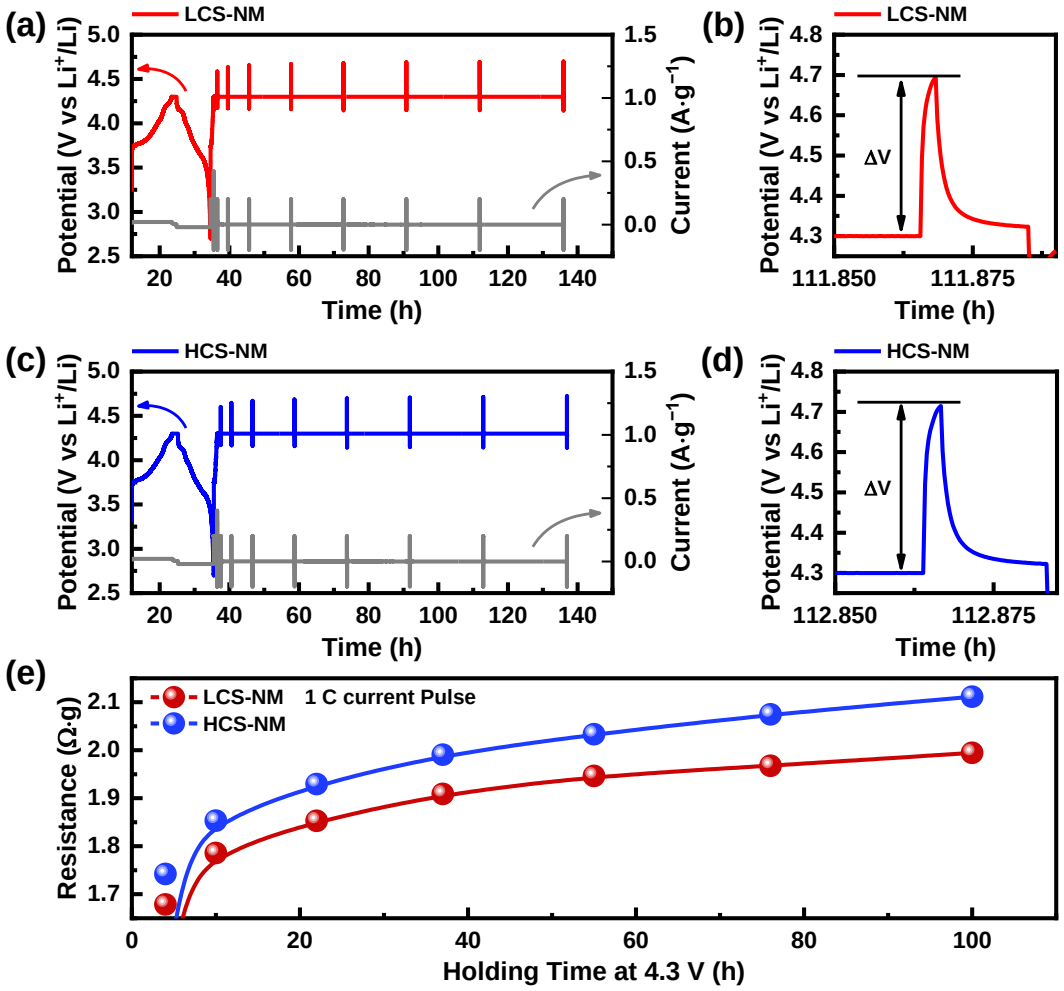

Fig. S37 Potential and current pulse profiles during the potential hold at 4.3 V for (a) LCS-NM and (c) HCS-NM cells. Direct current resistances (DCR) calculated using overpotential (ΔV) [(b), (d)] and current (I) based on Ohm's law. (e) HPPC test results at each holding time at 4.3 V.

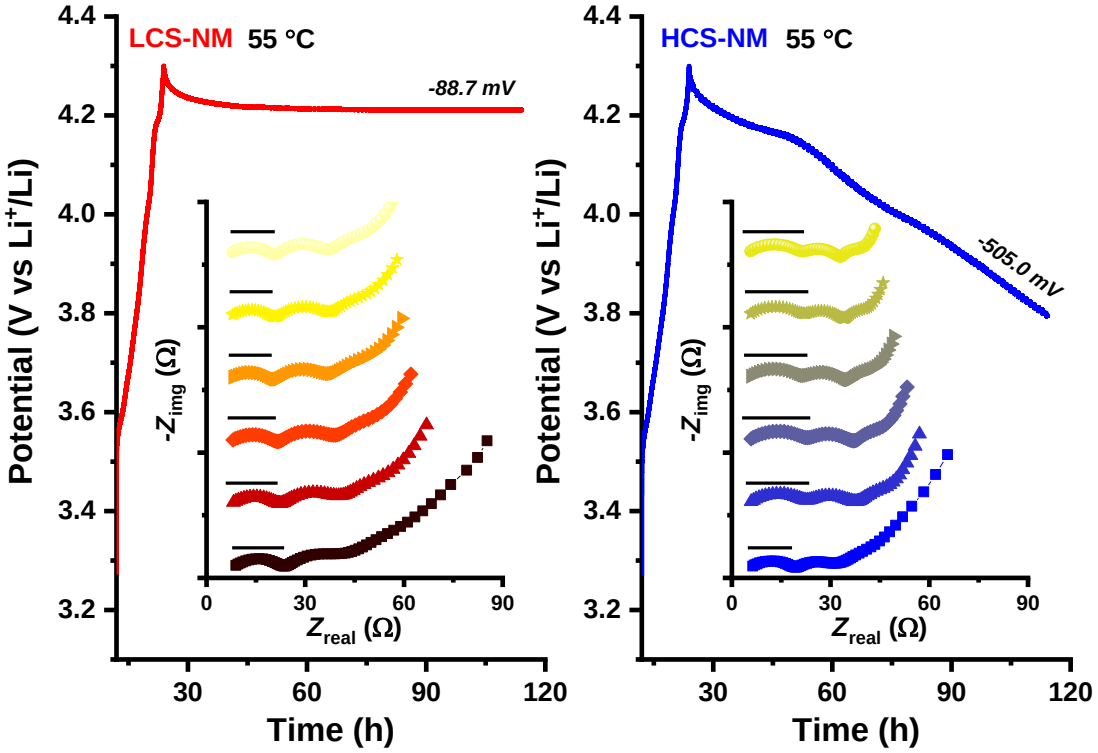

Fig. S38 OCV drop monitoring after charging to 4.3 V and Nyquist plots obtained every 1 h during self-discharge of LCS-NM and HCS-NM at 55 °C.

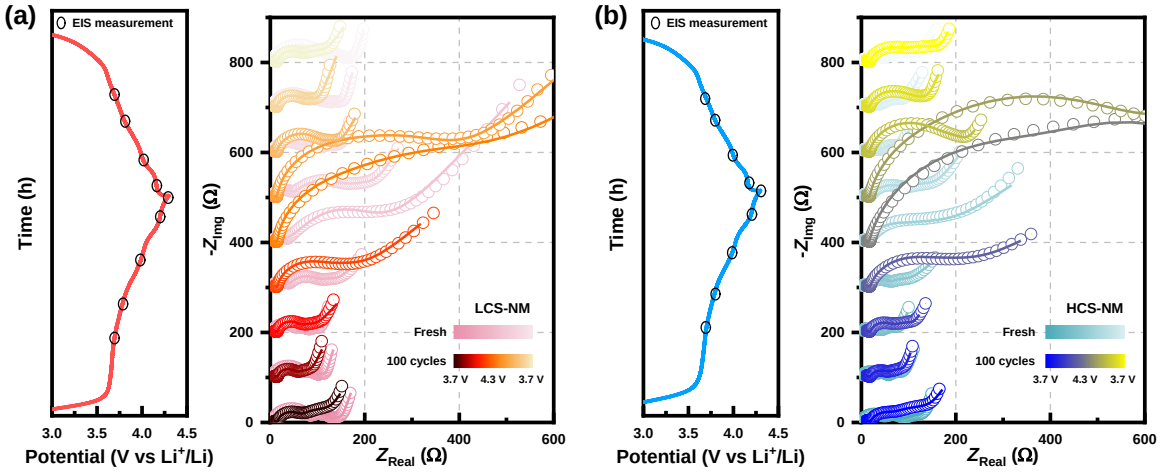

Fig. S39 Initial charge/discharge curves and corresponding in situ Nyquist plots at different potentials for fresh and 100-cycled half-cells employing **(a)** LCS-NM and **(b)** HCS-NM cathodes.

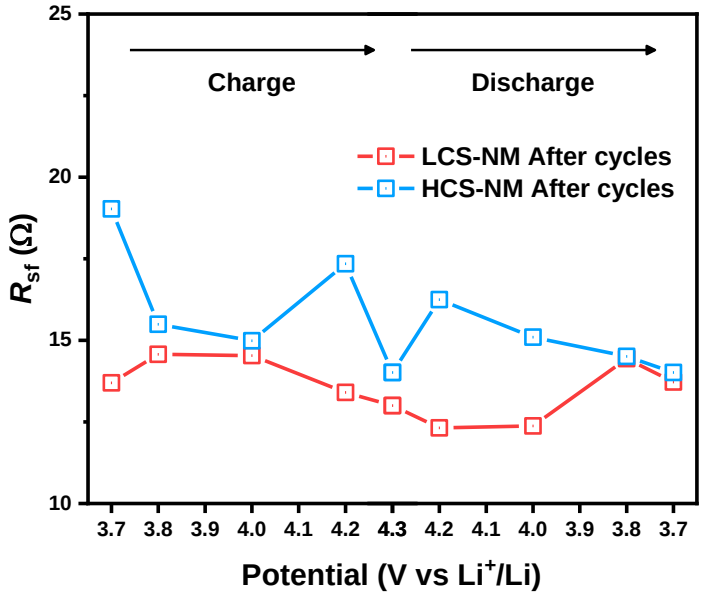

Fig. S40 Comparison of R_{sf} values at various potentials for LCS-NM and HCS-NM after long-term cycling.

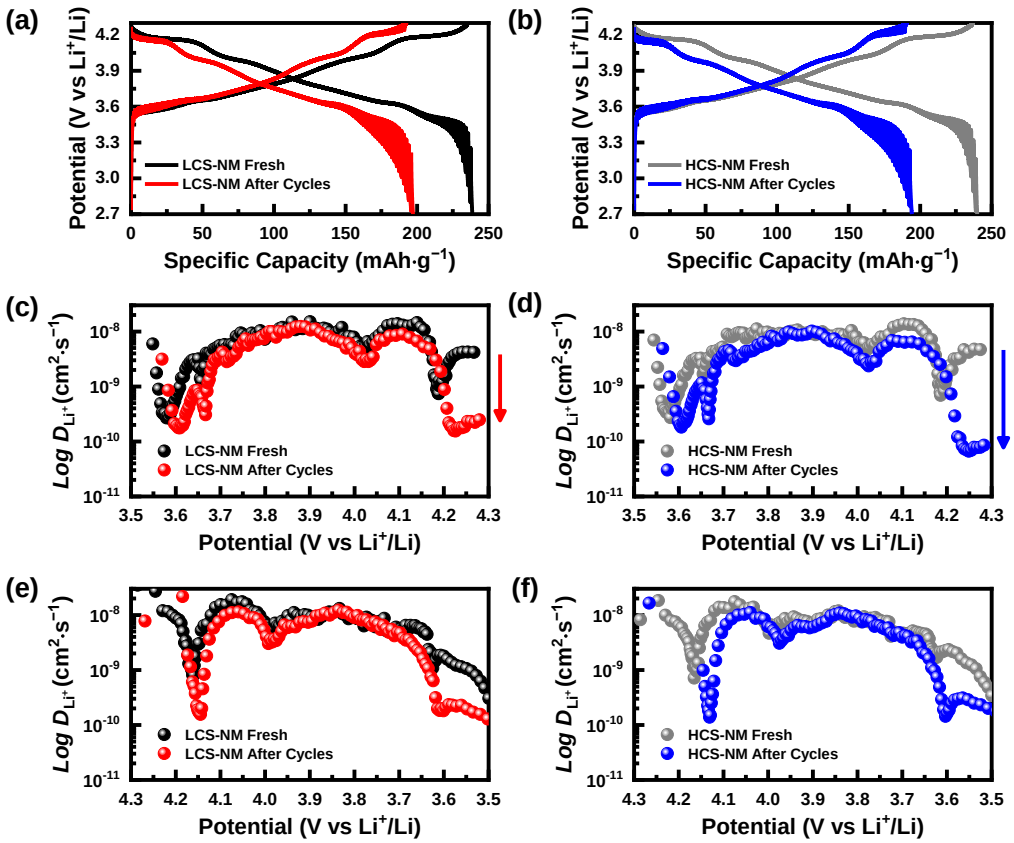

Fig. S41 Charge/discharge curves from GITT measurements for (a) LCS-NM and (b) HCS-NM cells before and after long-term cycling. Li-ion diffusion coefficients (D_{Li^+}) determined during charging for (c) LCS-NM and (d) HCS-NM, and during discharging for (e) LCS-NM and (f) HCS-NM, before and after long-term cycling.

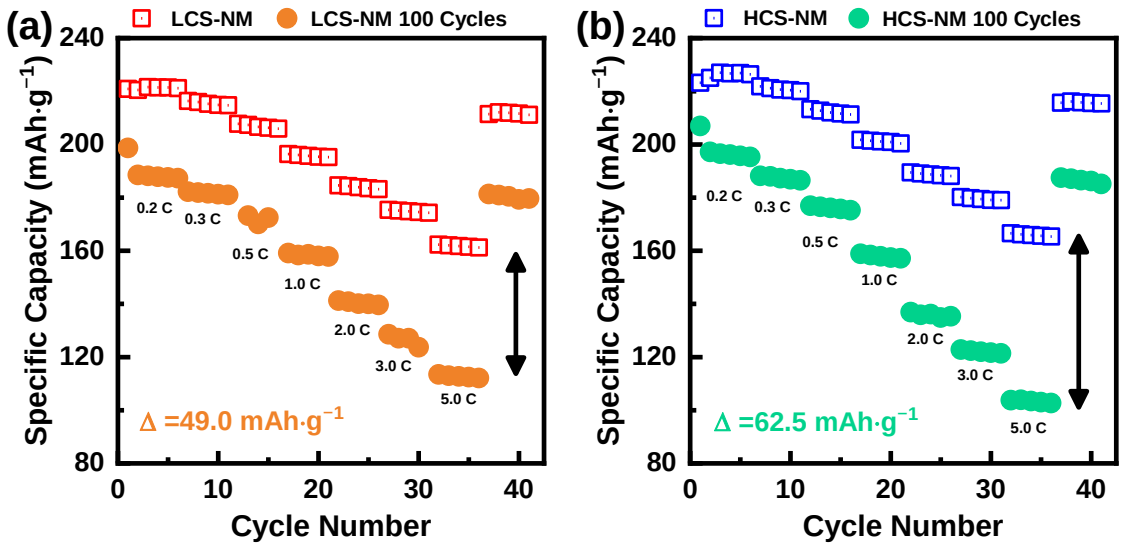

Fig. S42 Rate performance test results for (a) LCS-NM and (b) HCS-NM before and after long-term half-cell cycling.

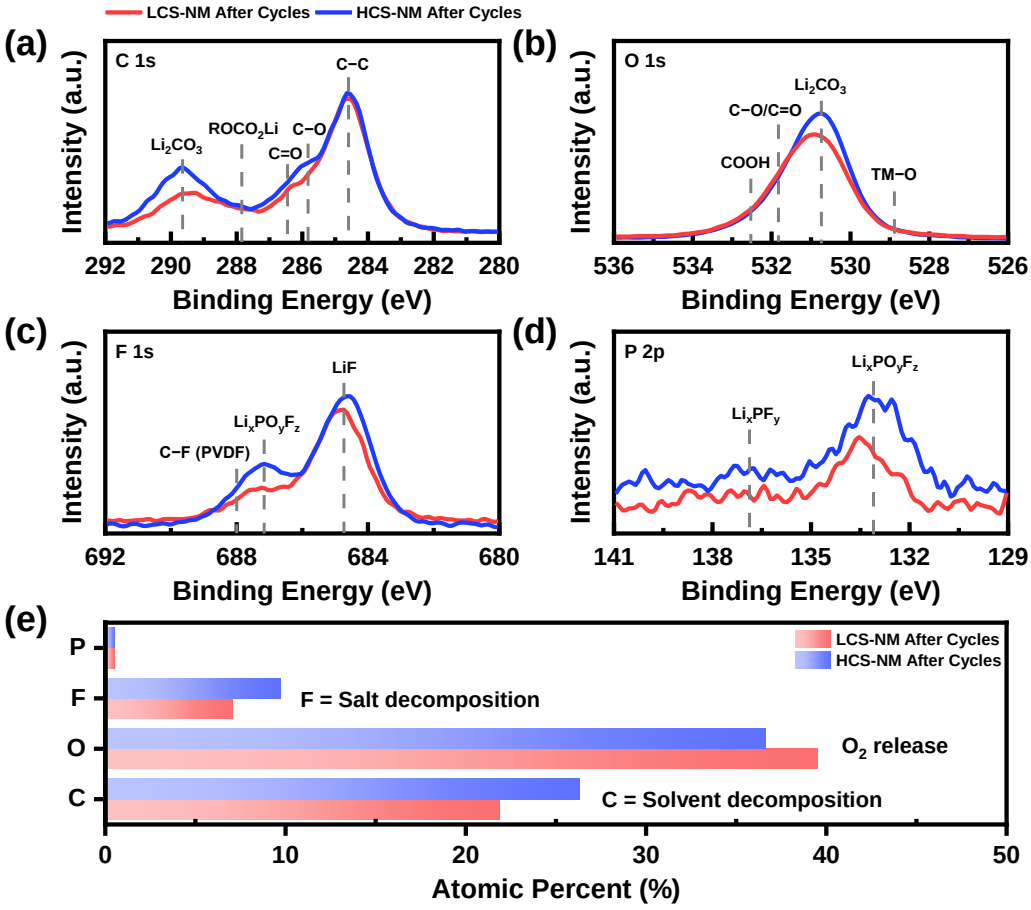

Fig. S43 (a) C 1s, (b) O 1s, (c) F 1s, and (d) P 2p XPS spectra of LCS-NM and HCS-NM electrodes after 100 cycles. (e) Atomic percentages of each component detected on the cathode electrodes after 100 cycles.

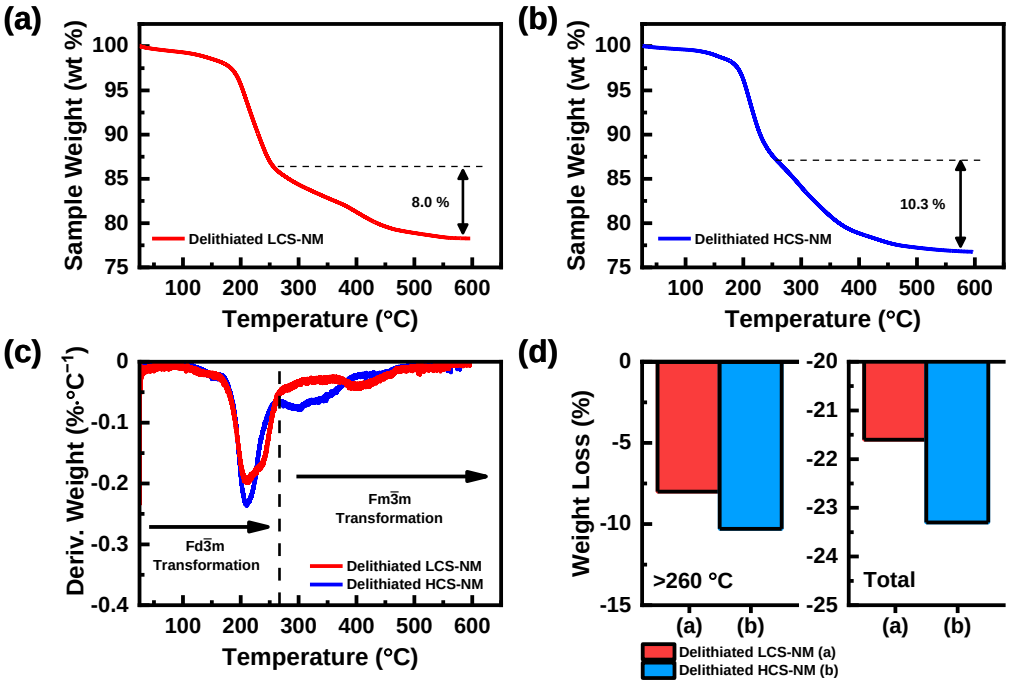

Fig. S44 TGA curves following chemical delithiation of (a) LCS-NM and (b) HCS-NM under an inert (N_2) atmosphere. (c) DTA curves derived from TGA and (d) relative weight loss above 260 °C comparing chemically delithiated LCS-NM and HCS-NM.

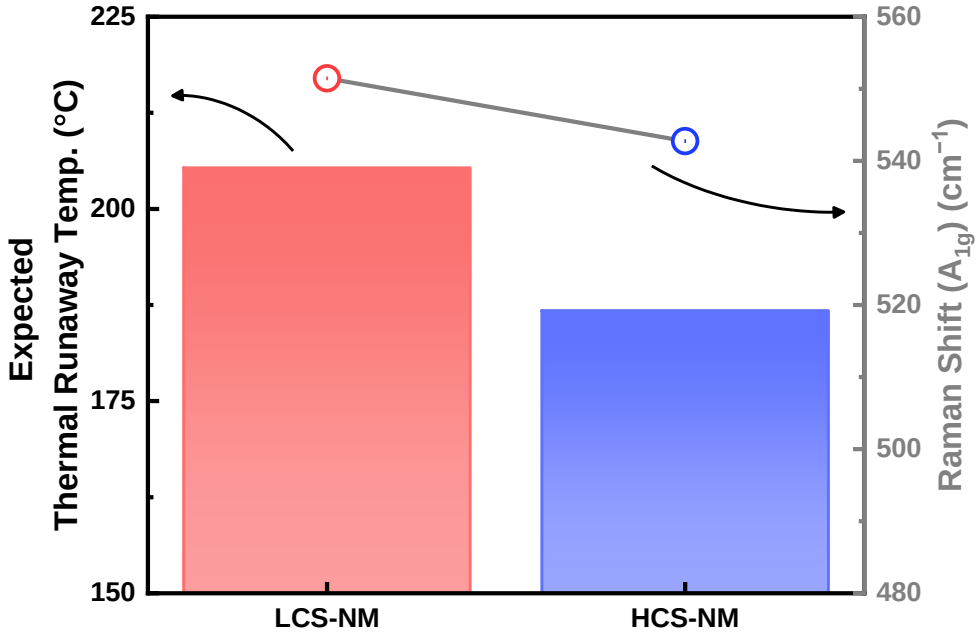

Fig. S45 Expected thermal runaway temperatures and Raman active A_{1g} shifts for LCS-NM and HCS-NM.

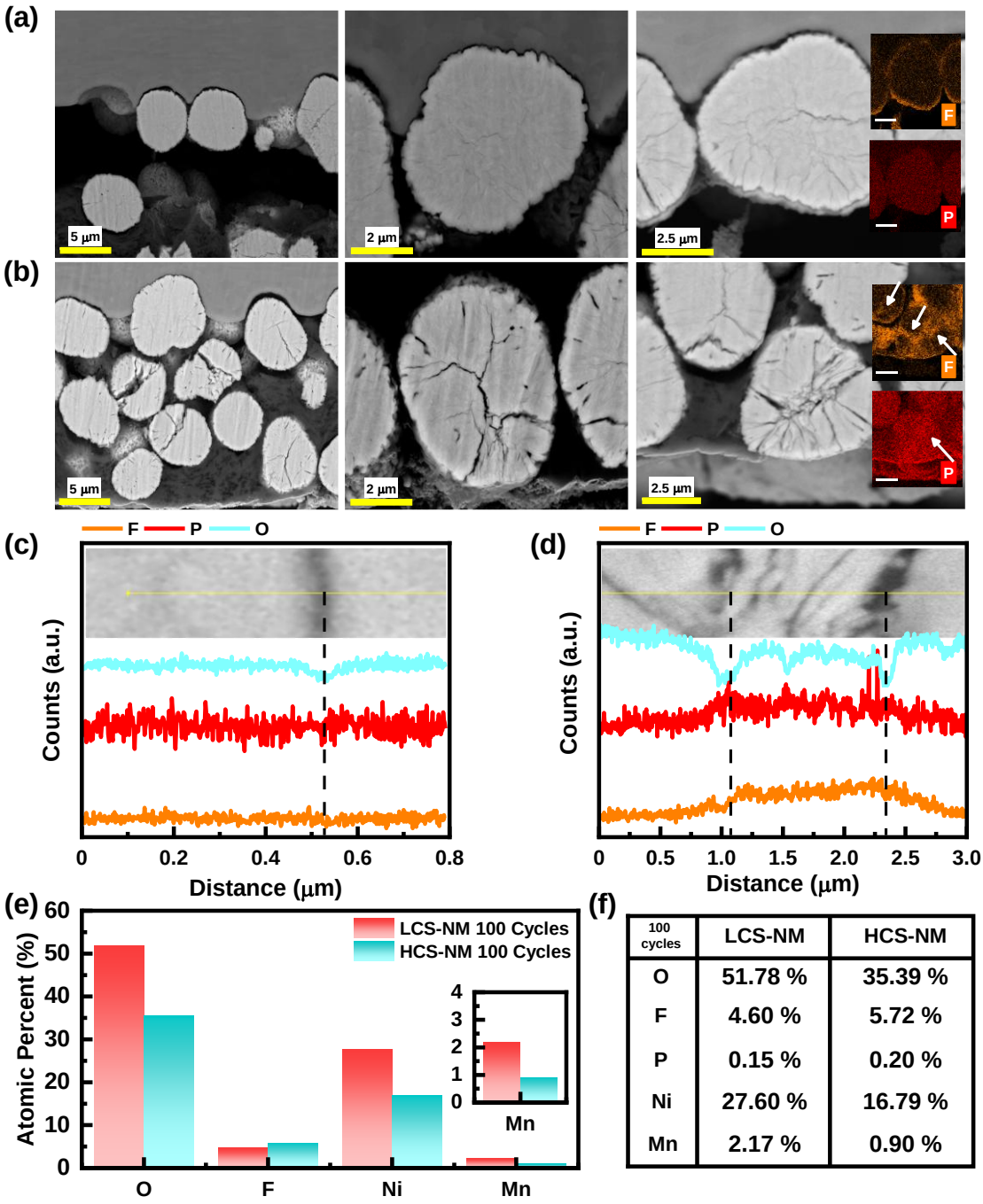

100 cycles	LCS-NM	HCS-NM
O	51.78 %	35.39 %
F	4.60 %	5.72 %
P	0.15 %	0.20 %
Ni	27.60 %	16.79 %
Mn	2.17 %	0.90 %

Fig. S46 Cross-sectional SEM images and EDS elemental maps (P, F) of (a) LCS-NM and (b) HCS-NM after 100 cycles. Arrows in the insets indicate differences in electrolyte penetration along particle cracks. Selected cross-sectional SEM images and EDS line profiles for O, P, and F of (c) LCS-NM and (d) HCS-NM after 100 cycles. (e, f) Atomic percentages of each element detected via EDS analysis for LCS-NM and HCS-NM after 100 cycles.

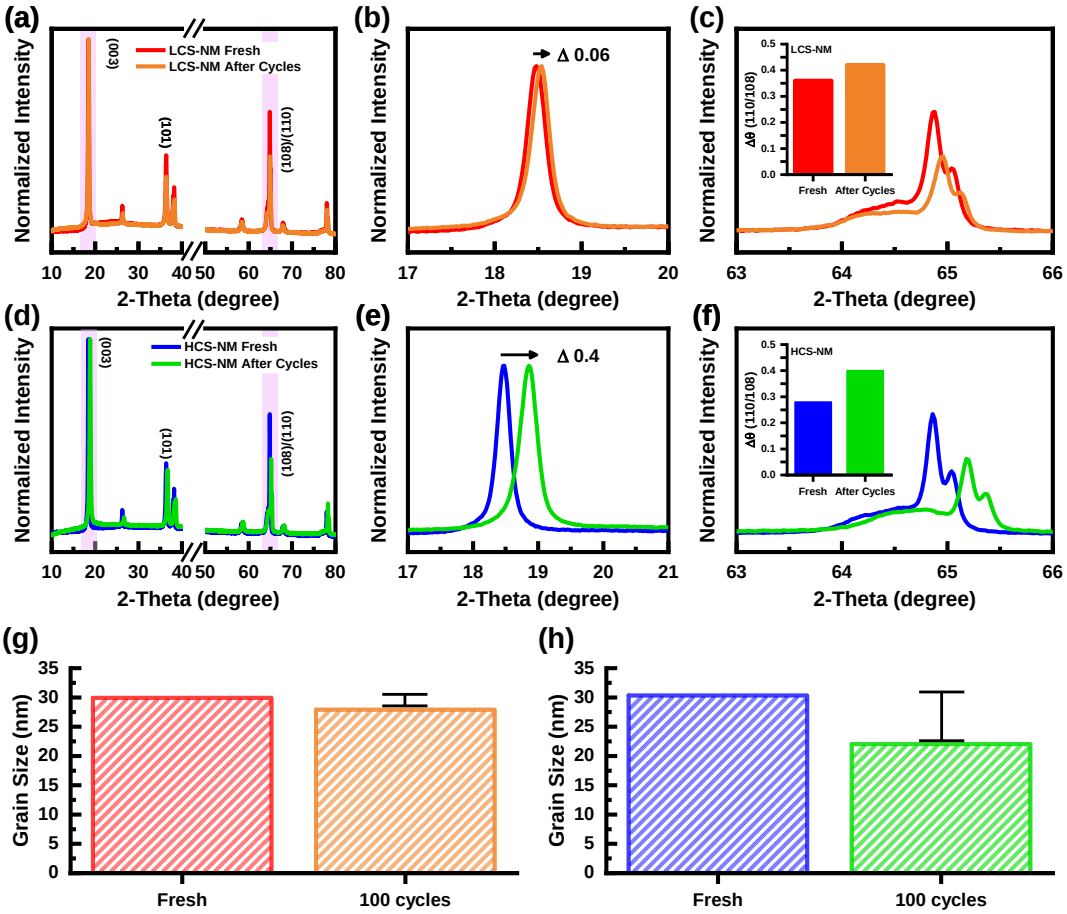

Fig. S47 XRD analysis results and magnified diffractograms in the 2-theta ranges of 17°–20° and 63°–66° for (a–c) LCS-NM and (d–f) HCS-NM electrodes before and after 100 cycles. Inset plots in (c) and (f) show the peak separation between the (110) and (108) planes before and after cycling. A larger shift in the (003) plane and a broader gap between the (108) and (110) planes in cycled HCS-NM indicate more severe layered collapse with the presence of the H3 phase and irreversible Li consumption, respectively.[1] Grain sizes of (g) LCS-NM and (h) HCS-NM before and after 100 cycles were calculated using the Scherrer equation, indicating finer particle cracking in the HCS-NM cathode.

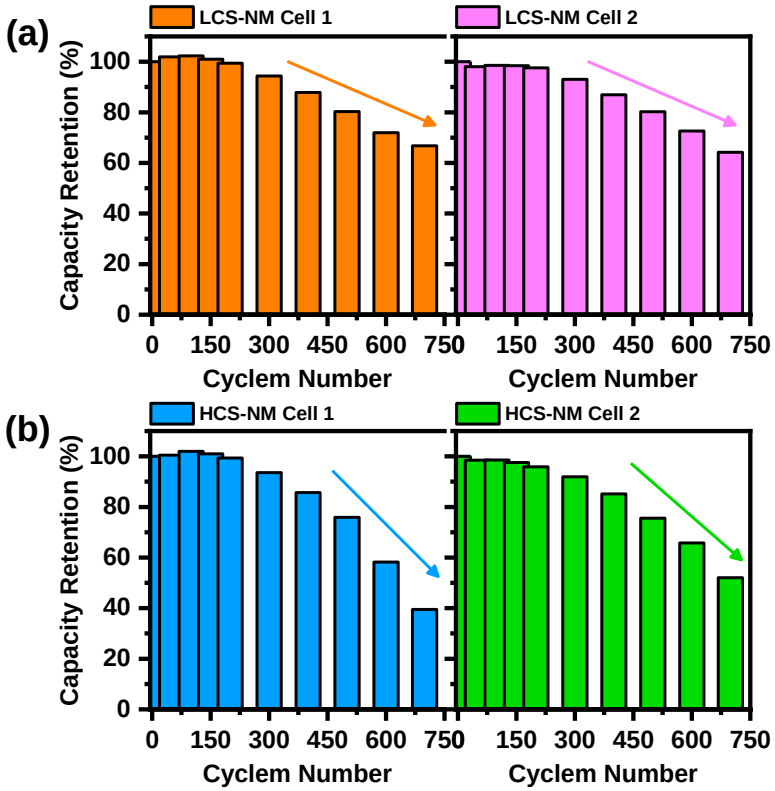

Fig. S48 Normalized capacity retention showing the reproducibility of (a) LCS-NM and (b) HCS-NM full cells.

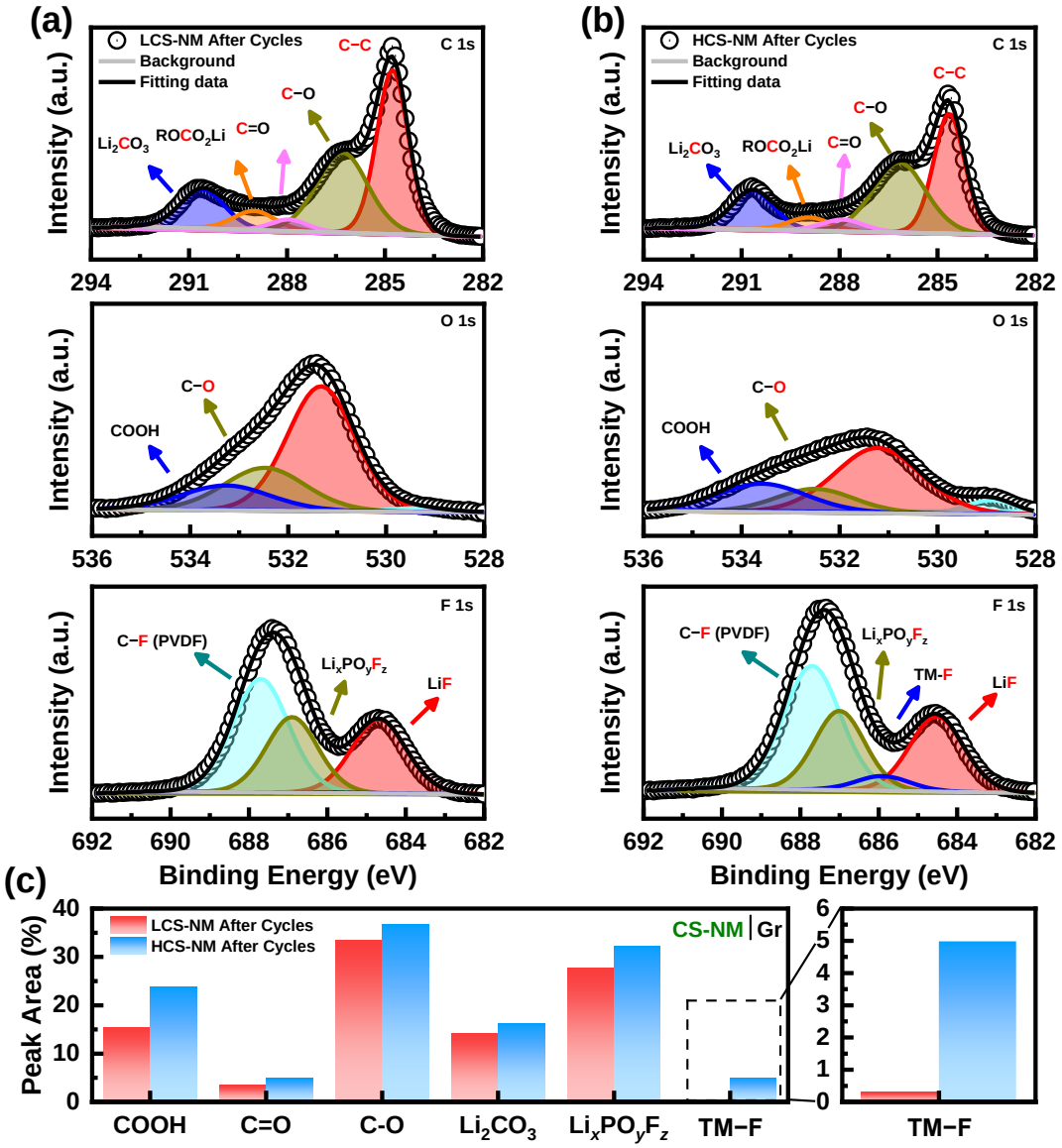

Fig. S49 C 1s, O 1s, and F 1s XPS spectra of (a) LCS-NM and (b) HCS-NM cathodes extracted from full cells after 700 cycles. (c) Relative peak areas of deconvoluted components.

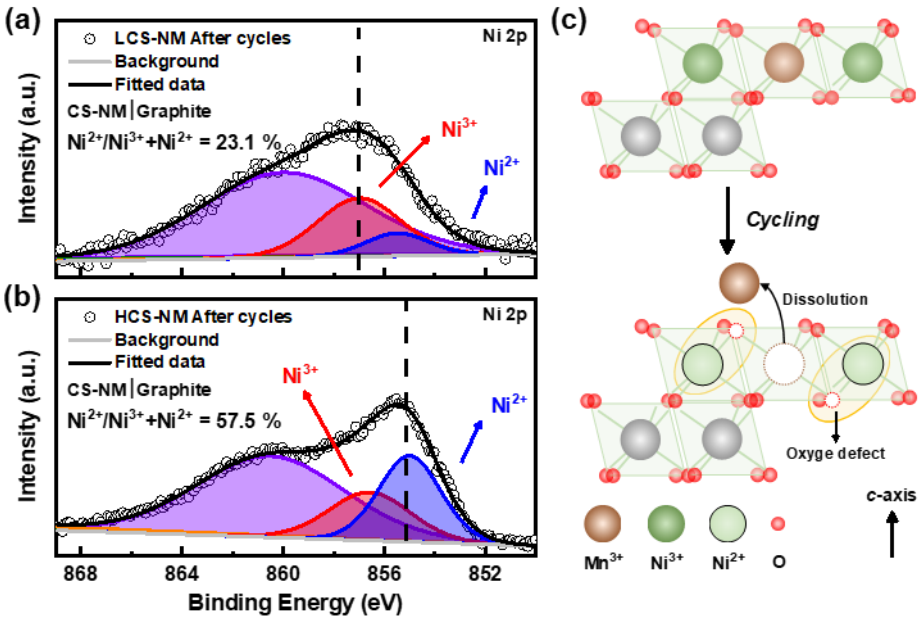

Fig. S50 Ni 2p XPS spectra of (a) LCS-NM and (b) HCS-NM cathodes extracted from full cells after 700 cycles. (c) Schematic illustration of the proposed Ni reduction mechanism driven by Mn dissolution and the loss of bonded oxygen shared within the Ni coordination environment.

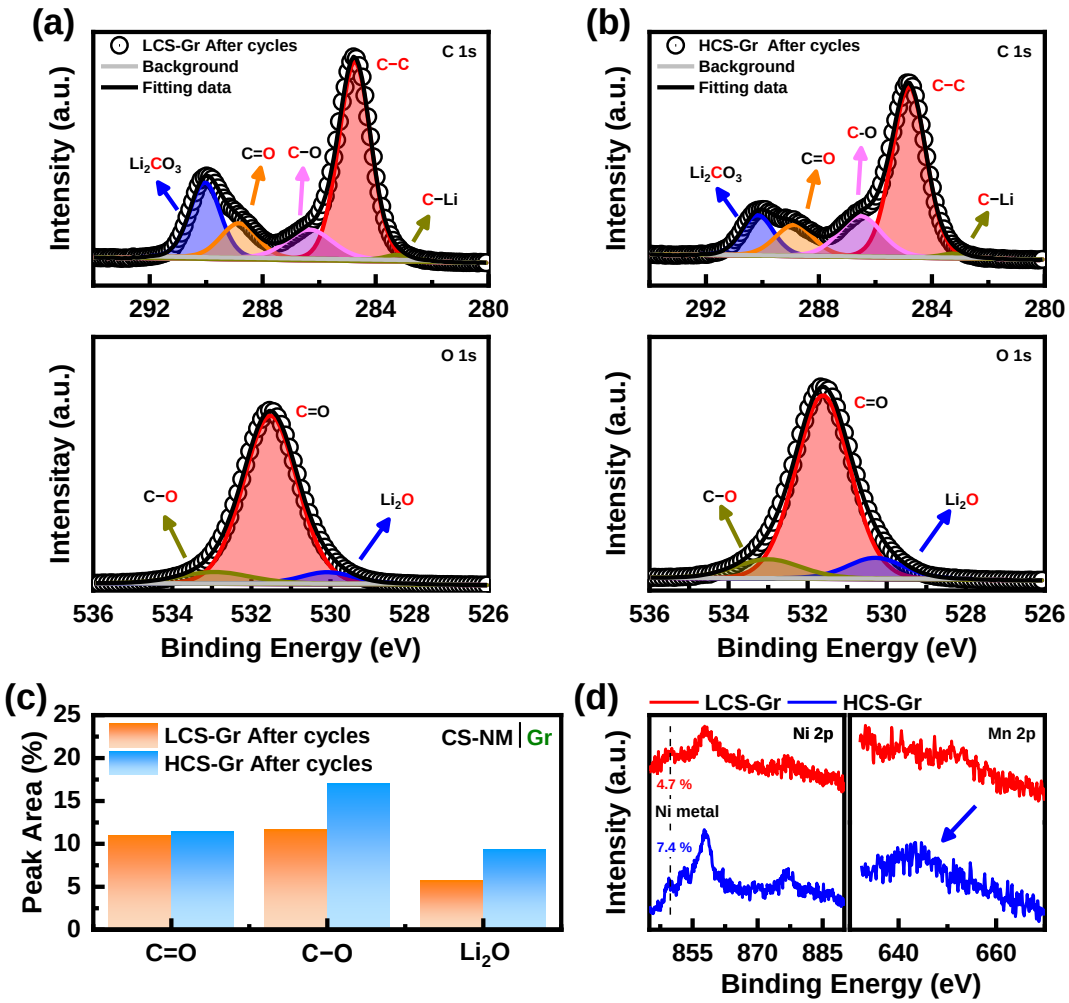

Fig. S51 C 1s and O 1s XPS spectra of graphite anodes (a) LCS-Gr and (b) HCS-Gr after 700 full-cell cycles paired with LCS-NM and HCS-NM cathodes, respectively. (c) Relative peak areas of deconvoluted components for each graphite anode. (d) Ni 2p and Mn 2p XPS spectra of LCS-Gr and HCS-Gr anodes.

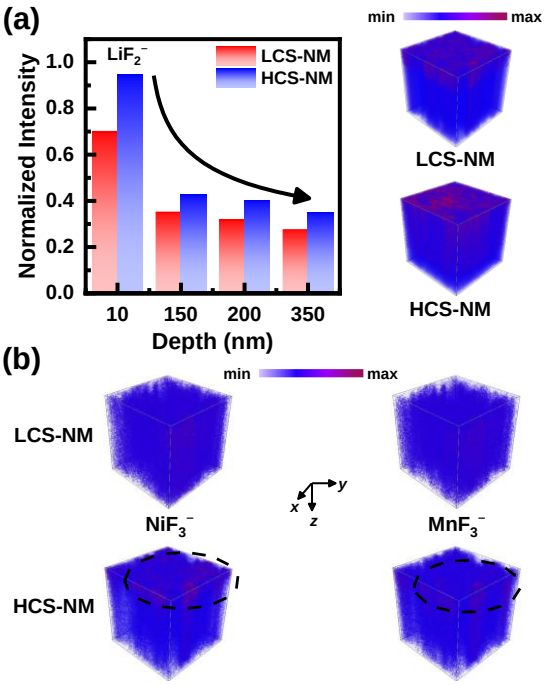

Fig. S52 (a) Normalized peak area of LiF_2^- (inorganic species) measured at different sputtering depths (10–350 nm) with corresponding 3D rendering images. (b) 3D rendering images of NiF_3^- and MnF_3^- fragments, attributed to transition metal dissolution from the cathode after 700 full-cell cycles.

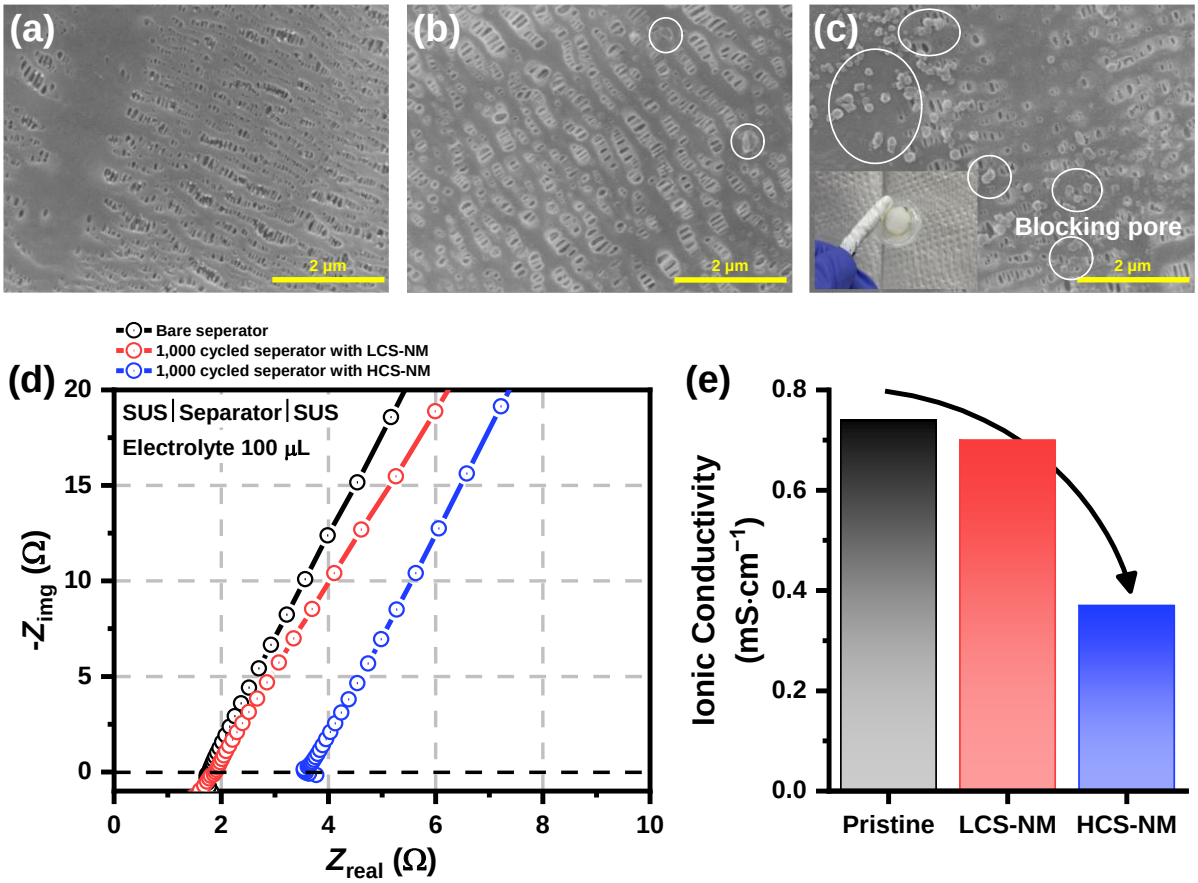

Fig. S53 SEM images of separators harvested from long-term cycled cells: (a) pristine, (b) LCS-NM, and (c) HCS-NM (Inset: Photograph showing color change in the separator after full-cell cycling). (d) Nyquist plots from blocking cells using each separator (pristine, cycled with LCS-NM, and HCS-NM) and (e) specific ionic conductivity calculated from EIS analysis using the following equation: $\sigma = \frac{l}{RA}$, where σ, R, A, and l represent ionic conductivity, bulk resistance, electrode area, and separator thickness, respectively.

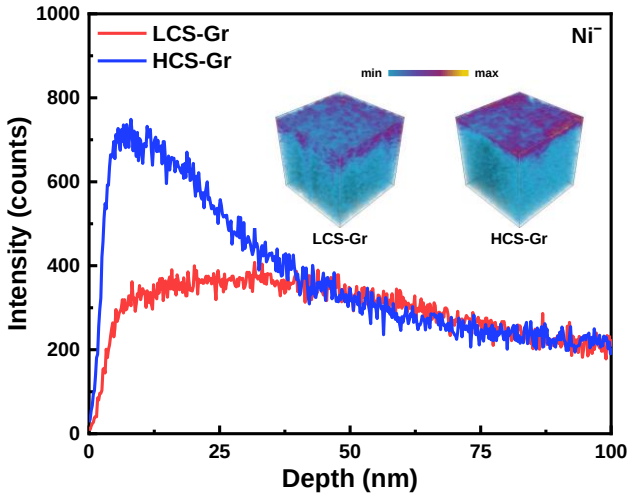

Fig. S54 TOF-SIMS Ni^- fragment spectra of graphite anodes paired with LCS-NM and HCS-NM cathodes after 700 full-cell cycles. Insets show 3D rendering images.

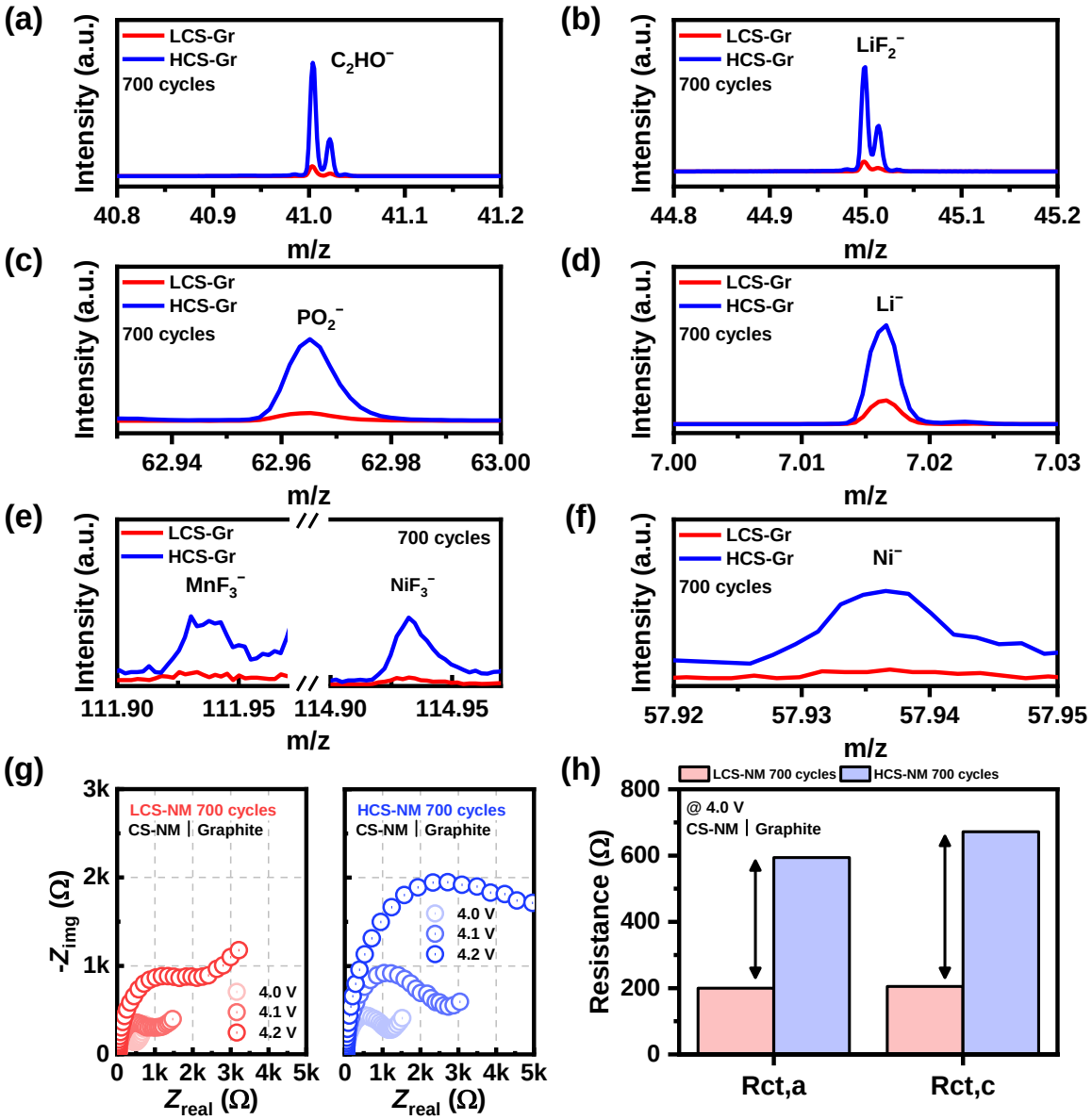

Fig. S55 Total loading spectra of (a) C_2HO^- and (b) LiF_2^- fragments representing organic and inorganic species, (c) PO_2^- fragments, (d) Li^- fragments representing Li dendritic species, (e) MnF_3^- and NiF_3^-, and (f) Ni^- secondary ions representing transition metals dissolved from the cathode and deposited in the SEI layer of graphite anodes after 700 cycles. (g) In situ EIS results for each full cell after 700 cycles and (h) calculated charge transfer resistance (R_{ct}) for both cathode ($R_{ct,c}$) and anode ($R_{ct,a}$) sides.

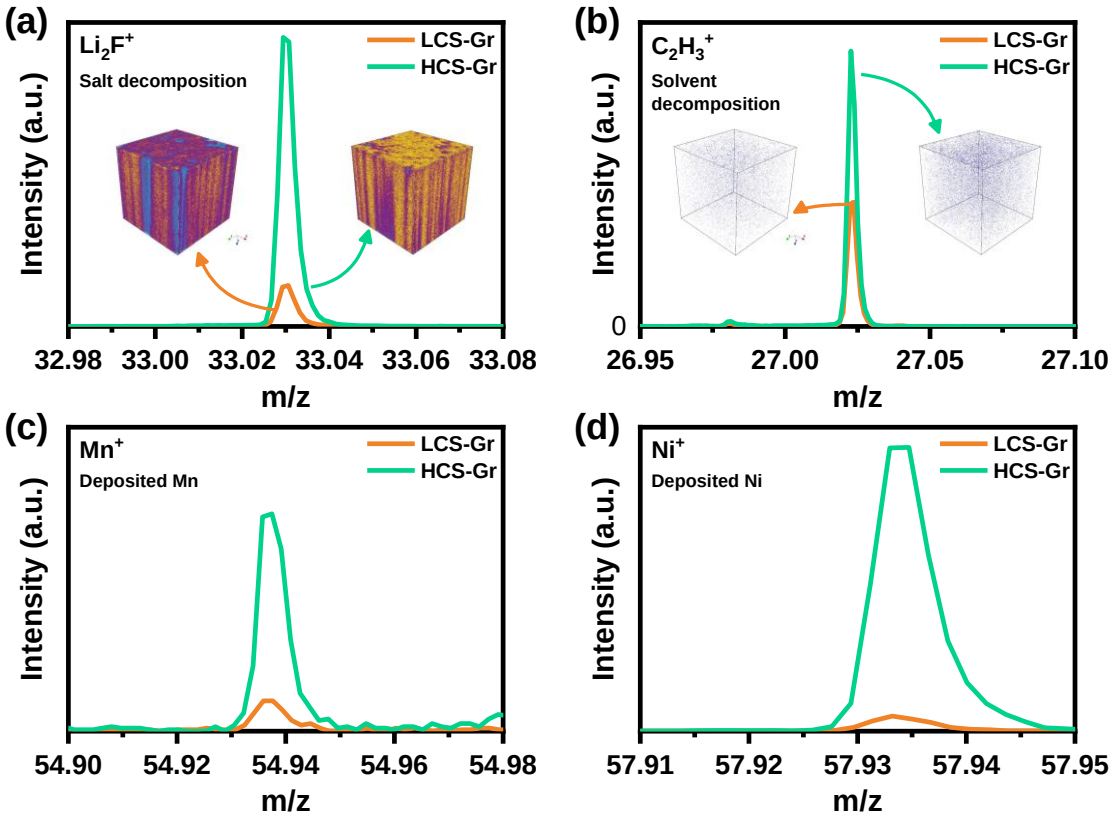

Fig. S56 Total loading spectra of (a) Li_2F^+ (inorganic species), (b) $C_2H_3^+$ (organic species), and (c, d) Mn^+ and Ni^+ deposited on the graphite anode. Insets: 3D structures represent 3D rendering images of Li_2F^+ and $C_2H_3^+$ fragments on graphite anodes, LCS-Gr (vs. LCS-NM) and HCS-Gr (vs. HCS-NM) after 1000 cycles.

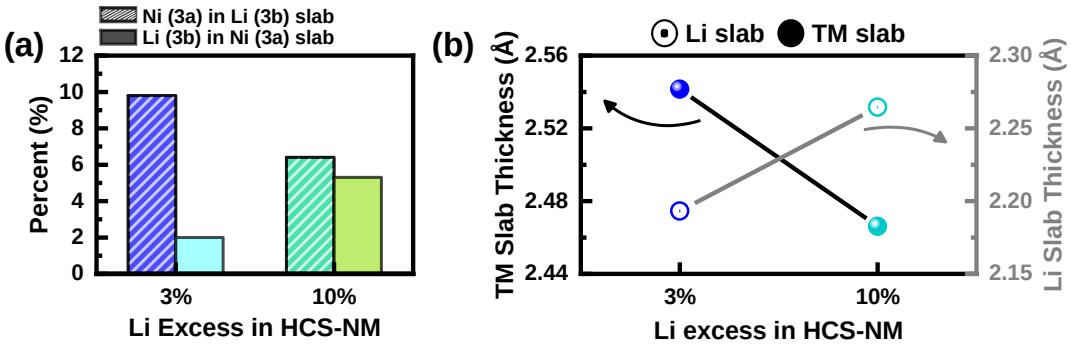

Fig. S57 Quantitative crystallographic fitting results: (a) Contents of Ni in Li slabs and Li in Ni slabs; (b) Interslab thickness of the TM slab and Li slab.

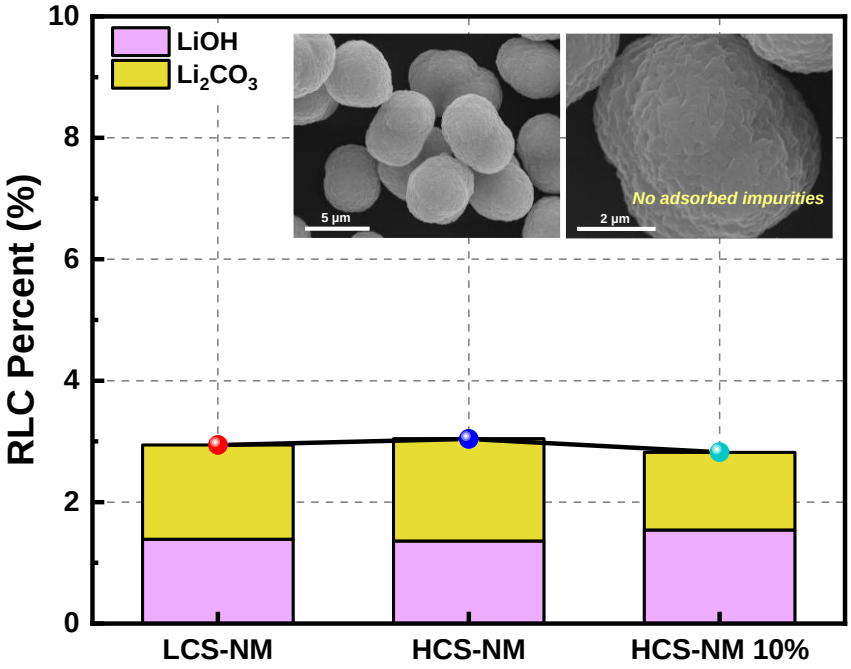

Fig. S58 Residual Li compound (RLC) concentrations determined by HCl titration for LCS-NM, HCS-NM, and HCS-NM (10% excess). Inset: SEM images of HCS-NM 10% at various magnifications.

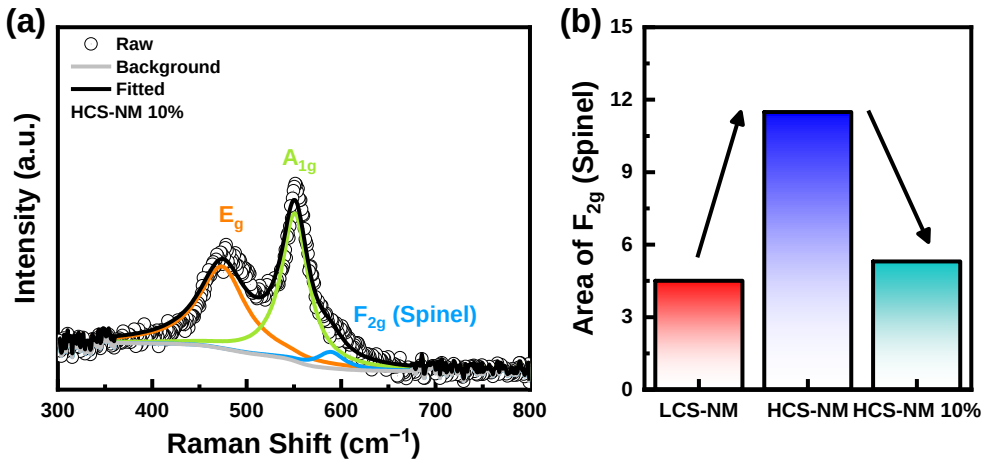

Fig. S59 (a) Gaussian fitting results of the Raman spectra for HCS-NM (10% excess). (b) Relative fraction of the F_{2g} mode (spinel structure) for LCS-NM, HCS-NM, and HCS-NM (10% excess).

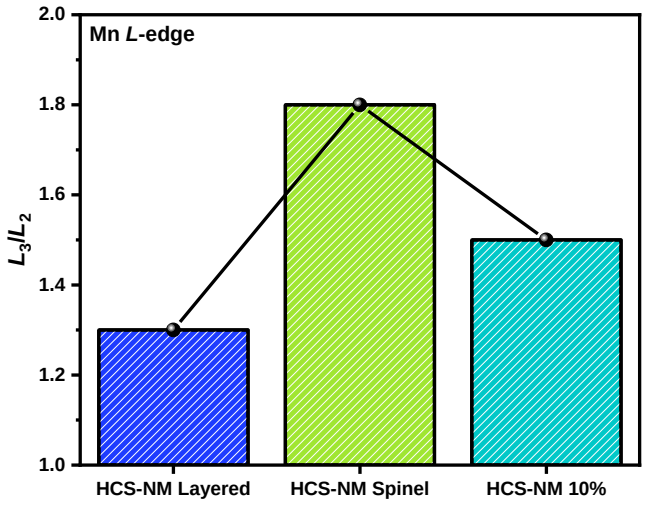

Fig. S60 Comparison of the Mn *L*-edge L_3/L_2 ratio for selected phases in HCS-NM and HCS-NM (10% excess).

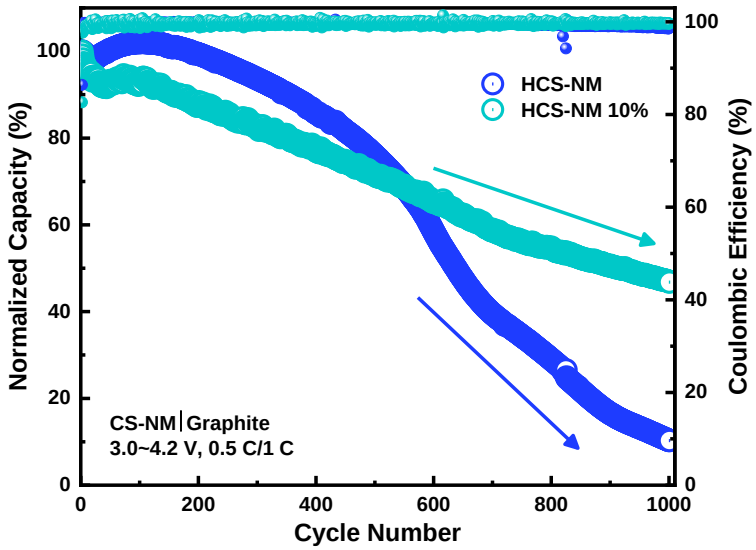

Fig. S61 Long-term cycling performance of full cells using HCS-NM and HCS-NM (10% excess) cathodes.

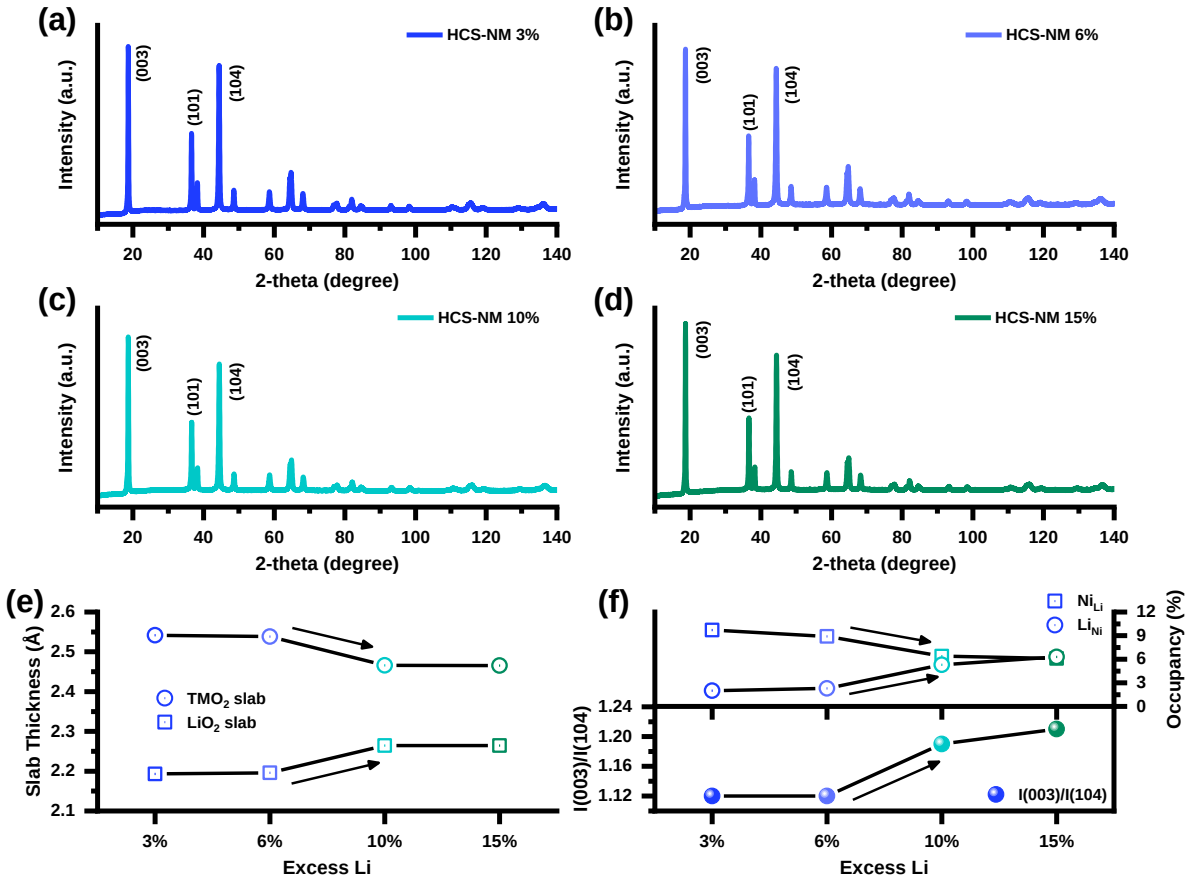

Fig. S62 XRD patterns of HCS-NM cathodes synthesized with varying amounts of excess Li: (a) 3%, (b) 6%, (c) 10%, and (d) 15%. Calculated (e) slab thicknesses and (f) site occupancies along with the I(003)/I(104) peak intensity ratios for the corresponding HCS-NM cathodes.

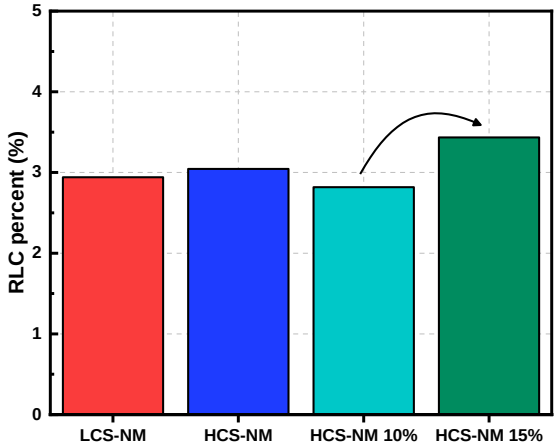

Fig. S63 Comparison of residual lithium compound (RLC) concentrations across the LCS-NM, HCS-NM, and modified HCS-NM (10% and 15%) samples.

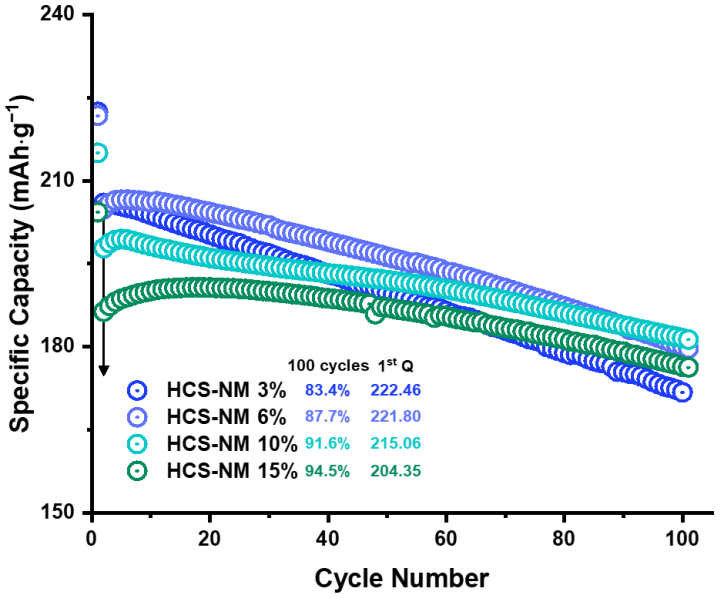

Fig. S64 Long-term cycling performance of HCS-NM with varying levels of lithium excess (3–15%) in half-cells.

Table S1 ICP-OES elemental analysis results for the prepared core/shell precursors. The data represent the average of duplicate measurements.

Core/shell cathode precursor	Ni (ppm)	Mn (ppm)	Stoichiometry
1st measurement	88.64	3.42	$Ni_{0.96}Mn_{0.04}$
2nd measurement	84.79	3.43	$Ni_{0.959}Mn_{0.041}$

Table S2 Crystallographic parameters obtained from Rietveld refinement.

LCS-NM	
a (Å)	2.8748
c (Å)	14.1998
T_{TMO_2} (Å)	2.4447
T_{LiO_2} (Å)	2.2885
R_{wp}	3.51

LCS-NM (Site)	x	y	z	Occ	B_{iso}
Ni in Ni (Ni1)	0	0	0.5	0.9617	0.5775
Ni in Li (Ni2)	0	0	0	0.07392	2.645
Li in Li (Li1)	0	0	0	0.9261	4.819
Li in Ni (Li2)	0	0	0.5	0.038232	1.623
O	0	0	0.24725	1	1.046

HCS-NM	
a (Å)	2.8761
c (Å)	14.2043
T_{TMO_2} (Å)	2.5415
T_{LiO_2} (Å)	2.1932
R_{wp}	3.03

HCS-NM (Site)	x	y	z	Occ	B_{iso}
Ni in Ni (Ni1)	0	0	0.5	0.9796	0.3196
Ni in Li (Ni2)	0	0	0	0.09723	2.587
Li in Li (Li1)	0	0	0	0.9028	7.778
Li in Ni (Li2)	0	0	0.5	0.02037	1.809
O	0	0	0.24387	1	0.2958

Table S3 Electronic configurations and crystal field stabilization energies (CFSE) for Ni and Mn ions. Calculated values are provided for octahedral crystal field stabilization energy (O_h CFSE), tetrahedral crystal field stabilization energy (T_d CFSE), and octahedral site stabilization energy (OSSE). Values are derived from crystal field theory and referenced from previous literature.[2]

Cation	Electron configuration	O_h CFSE	T_d CFSE	OSSE*
Ni^{3+}(LS*)	$t_{2g}^6\ e_g^1$	$-1.8\Delta_o$	$-0.54\Delta_t$	-1.26Δ
Ni^{2+}(LS)	$t_{2g}^6\ e_g^2$	$-1.2\Delta_o$	$-0.36\Delta_t$	-0.84Δ
Mn^{4+}(HS*)	t_{2g}^3	$-1.2\Delta_o$	$-0.36\Delta_t$	-0.84Δ
Mn^{3+}(HS)	$t_{2g}^3\ e_g^1$	$-0.6\Delta_o$	$-0.18\Delta_o$	-0.42Δ

* LS = Low spin

* HS = High spin

* OSSE = O_h CFSE – T_d CFSE

In octahedral (O_h) coordination, d-orbitals split into t_{2g} (stabilized by $-0.4\,\Delta_o$) and e_g (destabilized by $+0.6\Delta_o$).

Ni^{3+}: $6 \cdot (-0.4\Delta_o) + 1 \cdot (0.6\Delta_o) = -1.8\Delta_o$

Ni^{2+}: $6 \cdot (-0.4\Delta_o) + 2 \cdot (0.6\Delta_o) = -1.2\Delta_o$

Mn^{4+}: $3 \cdot (-0.4\Delta_o) = -1.2\Delta_o$

Mn^{3+}: $3 \cdot (-0.4\Delta_o) + 1 \cdot (0.6\Delta_o) = -0.6\Delta_o$

In tetrahedral (T_d) coordination, orbitals split into e_g (stabilized by $-0.6\Delta_t$) and t_{2g} (destabilized by $+0.4\Delta_t$). The relationship between the crystal field splitting parameters is approximated as $\Delta_t \approx \frac{4}{9}\Delta_o$. Calculations for specific ions are as follows:

Ni^{3+}: $4 \cdot (-0.6\Delta_t) + 3 \cdot (0.4\Delta_t) = -1.2\Delta_t \approx -0.54\Delta_o$

Ni^{2+}: $4 \cdot (-0.6\Delta_t) + 4 \cdot (0.4\Delta_t) = -0.8\Delta_t \approx -0.36\Delta_o$

Mn^{4+}: $2 \cdot (-0.6\Delta_t) + 1 \cdot (0.4\Delta_t) = -0.8\Delta_t \approx -0.36\Delta_o$

Mn^{3+}: $2 \cdot (-0.6\Delta_t) + 2 \cdot (0.4\Delta_t) = -0.4\Delta_t \approx -0.18\Delta_o$

Table S4 Theoretical and measured effective magnetic moments for the LCS-NM and HCS-NM cathodes and their corresponding deviations.

***$Ni^{3+}/Mn^{4+}/Ni^{2+}$**	**Theoretical μ_{eff}**	**Obtained μ_{eff}*** **	**Difference**
LCS-NM	2.02 μ_B	2.04 μ_B	0.02
****$Ni^{3+}/Mn^{3+}/Ni^{2+}$**	**Theoretical μ_{eff}**	**Obtained μ_{eff}*** **	**Difference**
HCS-NM	2.16 μ_B	2.13 μ_B	0.03

* Theoretical effective magnetic moment was calculated based on the molar concentration of each magnetic cation obtained from Rietveld refinement.

** Theoretical values were calculated based on $Ni^{3+}/Mn^{4+}/Ni^{2+}$ cation combinations for LCS-NM and $Ni^{3+}/Mn^{3+}/Ni^{2+}$ cation combinations for HCS-NM. Because it is challenging to determine the exact concentration of Mn^{3+}, we assumed that all Mn cations were reduced to Mn^{3+} as a theoretical limiting case to establish an upper bound.

*** All theoretical value calculations follow the general equation: $\mu_{eff} = \sqrt{\sum_i n_i \cdot (u_{eff,i})^2}$

Table S5 Observed ^{13}C and ^{19}F NMR chemical shifts in non-aqueous electrolytes.

Nucleus	Chemical shift (ppm)	Assignment
^{13}C*	156.58 (s) / 156.60 (s) / 156.72 (s)	C=O in EC
	156.36 (s) / 156.41 (s)	C=O in DMC
	155.17 (s) / 155.22 (s)	C=O in DEC
	65.26 (s) / 65.31 (s)	O–CH_3 in DMC
	63.55 (s) / 63.61 (s)	O–CH_2 in DEC
	54.31 (s) / 54.33 (s) / 54.35 (s)	CH_2 in EC
	13.33 (s) / 13.3 (s)	CH_3 in DEC
	38 (septet)	DMSO-d_6
^{19}F	–72.61	PF_6^- (coordination 1)
	–74.7	PF_6^- (coordination 2)
	–82.98	$POF_2(OH)$
	–85.44	$POF_2(OH)$
	–83.14	$POF_2(OR)$ (R=alkyl)
	–85.61	$POF_2(OR)$ (R=alkyl)
	around –155	hydrolysis F^-

* Variations in chemical shifts reflect the alteration of the solvation shell structure during aging. Data are color-coded: black for pristine electrolyte, red for aged electrolyte with LCS-NM, and blue for aged electrolyte with HCS-NM.

Table S6 Crystallographic parameters derived from the Rietveld refinement of the HCS-NM 10% sample.

HCS-NM 10%	
a (Å)	2.8707
c (Å)	14.1922
T_{TMO_2} (Å)	2.4661
T_{LiO_2} (Å)	2.2646
R_{wp}	2.91

HCS-NM 10% (Site)	*x*	*y*	*z*	Occ	B_{iso}
Ni in Ni (Ni1)	0	0	0.5	0.947	0.5397
Ni in Li (Ni2)	0	0	0	0.06422	6.668
Li in Li (Li1)	0	0	0	0.9358	2.008
Li in Ni (Li2)	0	0	0.5	0.05301	0.8847
O	0	0	0.24645	1	0.8528

Table S7 Crystallographic parameters derived from the Rietveld refinement of the HCS-NM 3% sample.

HCS-NM 3%	
a (Å)	2.8761
c (Å)	14.2043
T_{TMO_2} (Å)	2.5415
T_{LiO_2} (Å)	2.1932
R_{wp}	3.13

HCS-NM 3% (Site)	*x*	*y*	*z*	Occ	B_{iso}
Ni in Ni (Ni1)	0	0	0.5	0.9796	0.3196
Ni in Li (Ni2)	0	0	0	0.09723	2.587
Li in Li (Li1)	0	0	0	0.9028	7.778
Li in Ni (Li2)	0	0	0.5	0.020371	1.809
O	0	0	0.24387	1	0.2958

Table S8 Crystallographic parameters derived from the Rietveld refinement of the HCS-NM 6% sample.

HCS-NM 6%	
a (Å)	2.8755
c (Å)	14.2028
T_{TMO_2} (Å)	2.5381
T_{LiO_2} (Å)	2.1961
R_{wp}	2.544

HCS-NM 6% (Site)	*x*	*y*	*z*	Occ	B_{iso}
Ni in Ni (Ni1)	0	0	0.5	0.977	0.458
Ni in Li (Ni2)	0	0	0	0.08912	6.422
Li in Li (Li1)	0	0	0	0.9109	0.5991
Li in Ni (Li2)	0	0	0.5	0.02304	2.614
O	0	0	0.24398	1	0.1758

Table S9 Crystallographic parameters derived from the Rietveld refinement of the HCS-NM 15% sample.

HCS-NM 15%	
a (Å)	2.8701
c (Å)	14.1890
T_{TMO_2} (Å)	2.4653
T_{LiO_2} (Å)	2.2644
R_{wp}	2.49

HCS-NM 15% (Site)	*x*	*y*	*z*	Occ	B_{iso}
Ni in Ni (Ni1)	0	0	0.5	0.937	0.2118
Ni in Li (Ni2)	0	0	0	0.0607	7.628
Li in Li (Li1)	0	0	0	0.9393	1.391
Li in Ni (Li2)	0	0	0.5	0.06301	7.124
O	0	0	0.24646	1	0.8447

References

1 Z. Cui, Q. Xie and A. Manthiram, *Adv. Energy Mater.*, 2021, **11**, 2102421.

2 Z. Cui, P. Zuo, Z. Guo, C. Wang and A. Manthiram, *Adv. Mater.*, 2024, **36**, 2402420.